applied sciences

MDPI

Article

System-Level Assessment of a C-RAN Based on Generalized Space–Frequency Index Modulation for 5G New Radio and Beyond

Vasco Velez [1,2,*], João Pedro Pavia [1,2], Catarina Rita [1], Carolina Gonçalves [1], Nuno Souto [1,2], Pedro Sebastião [1,2] and Américo Correia [1,2]

[1] Department of Information Science and Technology, ISCTE-Instituto Universitário de Lisboa, 1649-026 Lisbon, Portugal; Joao_Pedro_Pavia@iscte-iul.pt (J.P.P.); Catarina_Rita@iscte-iul.pt (C.R.); Carolina_Loureiro@iscte-iul.pt (C.G.); Nuno.Souto@iscte-iul.pt (N.S.); Pedro.Sebastiao@iscte-iul.pt (P.S.); Americo.Correia@iscte-iul.pt (A.C.)

[2] Instituto de Telecomunicações, 1049-001 Lisbon, Portugal

* Correspondence: Vasco_Velez@iscte-iul.pt

Abstract: Index modulation (IM) has been attracting considerable research efforts in recent years as it is considered a promising technology that can enhance spectral and energy efficiency and help cope with the rising demand of mobile traffic in future wireless networks. In this paper, we propose a cloud radio access network (C-RAN) suitable for fifth-generation (5G) and beyond systems, where the base stations (BSs) and access points (APs) transmit multidimensional IM symbols, which we refer to as precoding-aided transmitter-side generalized space–frequency IM (PT-GSFIM). The adopted PT-GSFIM approach is an alternative multiuser multiple-input multiple-output (MU-MIMO) scheme that avoids multiuser interference (MUI) while exploiting the inherent diversity in frequency-selective channels. To validate the potential gains of the proposed PT-GSFIM-based C-RAN, a thorough system-level assessment is presented for three different three-dimensional scenarios taken from standardized 5G New Radio (5G NR), using two different numerologies and frequency ranges. Throughput performance results indicate that the 28 GHz band in spite of its higher bandwidth and higher achieved throughput presents lower spectral efficiency (SE). The 3.5 GHz band having lower bandwidth and lower achieved throughput attains higher SE. Overall, the results indicate that a C-RAN based on the proposed PT-GSFIM scheme clearly outperforms both generalized spatial modulation (GSM) and conventional MU-MIMO, exploiting its additional inherent frequency diversity.

Keywords: index modulation; precoding; PT-GSFIM; multiuser MIMO; system-level simulation; 5G and beyond 5G

Citation: Velez, V.; Pavia, J.P.; Rita, C.; Gonçalves, C.; Souto, N.; Sebastião, P.; Correia, A. System-Level Assessment of a C-RAN Based on Generalized Space–Frequency Index Modulation for 5G New Radio and Beyond. *Appl. Sci.* **2022**, *12*, 1592. https://doi.org/10.3390/app12031592

Academic Editor: Mario Marques Da Silva

Received: 12 January 2022
Accepted: 31 January 2022
Published: 2 February 2022

1. Introduction

As technology advances in wireless communications, more innovative solutions have been appearing. These solutions should be able to handle the increase in the number of devices connected to the network and also the number of mobile traffic services that are growing day by day. Newer generations are expected to offer better system robustness, higher mobility and better spectral and energy efficiency than previous ones.

Current fifth-generation (5G) technology is capable, efficient and flexible, but can be improved further. 5G technology works in bands below 7 GHz, which corresponds to the Frequency Range 1 (FR1) of 5G New Radio (5G NR) [1], and above 24 GHz, corresponding to Frequency Range 2 (FR2) of 5G NR, and can accommodate many more users than the last generation counterpart. It uses the massive multiple-input multiple-output (MIMO) concept which allows achieving 100x higher efficiency without requiring more base stations (BSs). Massive MIMO and nonorthogonal multiple access (NOMA) are widely used in

wideband networks and can accommodate a higher number of users and streams but fail to achieve a higher spectral efficiency (SE) that is required to meet the challenges and requirements of beyond 5G (B5G) and future generations (6G) [2,3]. Regarding recent research work that has been done in the physical layer, one of the potential candidates to improve future and current networks is the use of index modulation (IM) schemes [4,5].

IM has surged in recent years as a promising technique to convey additional information bits, named index bits, that are distributed through a certain order and select certain resource elements such as antennas, subcarriers, slots and channels. This capability of activating certain resources of communications, through the indices of the building blocks, can result in improvements in energy efficiency (EE) and SE and also reduces the complexity of the receivers [3,6]. IM can be applied together with current technologies such as massive MIMO and can be used in high-mobility scenarios, such as mobile communications [5]. Spatial modulation (SM) and orthogonal frequency division multiplexing with IM (OFDM-IM) schemes are well-known examples of IM schemes [4,7].

SM was first introduced in order to simplify the MIMO schemes to a lower computational complexity and implementation, as it only requires a single RF chain to convey the index bits [8]. This type of scheme can be combined with conventional modulation techniques such as amplitude and phase modulation (APM), phase-shift keying (PSK) or quadrature amplitude modulation (QAM). Although SM only uses one active transmitter, in [9] the concept of SM was generalized to enable multiple active antennas simultaneously, which was named generalized SM (GSM). IM schemes such as SM and GSM are usually more suitable in large-scale communications, allowing superior EE and better BER results than conventional MIMO [5,9,10]. The addition of precoding techniques allows the implementation of SM relying on the activation of antennas at the receiver instead of the transmitter, enabling lower implementation complexity at the receiver [10].

OFDM-IM uses an alternative approach as it explores IM applied at the frequency domain instead of the spatial domain, relying on the indices of subcarriers of conventional OFDM transmission [11,12]. Like SM/GSM, in OFDM-IM only a portion of subcarriers are activated according to their indices, and only those convey M-ary modulated signals [13]. Various authors have modified and improved the basic OFDM-IM scheme. An example is using precoding techniques to improve further the communications in downlink between BSs and receivers. This results in reduced complexity at the receiver side, which tends to lower the interference [14]. The use of interleavers on OFDM subcarriers is another possible approach for achieving considerable improvements. In [15], the authors compared the performance of OFDM-IM with a subcarrier-level block interleaver (OFDM-ISIM) against traditional OFDM and OFDM-IM. It was shown that the former was capable of achieving better BER results. Layered OFDM-IM (L-OFDM-IM) is another example of an IM scheme that divides the OFDM subcarriers into multiple layers [16]. Dual-mode OFDM-IM (DM-OFDM-IM) and multimode OFDM-IM (MM-OFDM-IM) and their generalized versions are other good examples of IM-based OFDM schemes. Both of these schemes use groups of designed constellations, which can be selected according to their indices and desired communication [17–20]. All of these mentioned schemes tried to improve SE over OFDM-IM.

It is important to note that IM can also be applied to time and channel domains. In [21], the authors presented a scheme where IM is applied in the time domain. It uses the concept of time slots, similar to time-division multiple access (TDMA), which is named IM multiple access (IMMA). On the other hand, the IM approach in [22] uses the channel approach to convey additional information through channel realizations. This is also known as media-based modulation (MBM).

Many recent works on IM are focused on multiuser (MU) communications, especially in downlink situations. The receivers usually have a limited number of antennas, which are prone to multiuser interference (MUI). On the other hand, the uplink has less complexity and can be addressed like an extension of GSM [23]. Some authors have proposed versions of IM based on multidimensional schemes, which are built with a combination of spatial

and frequency domains [7]. In [24], the authors have merged both SM and OFDM-IM schemes simultaneously to produce a scheme named generalized space–frequency IM (GSFIM). In this new technique, the index bits can select which antenna and subcarrier should be activated at each transmission. Although only single user (SU) cases were explored, the authors showed good results in BER performance and transmission rates, when compared with other schemes. More recently, in [25] the authors extended the same concept, proposing multidimensional IM schemes that work in MU scenarios. Both frequency and spatial domains are exploited for downlink MU communications with the assistance of signal space diversity (SSD), showing promising results. In [26], a scheme that combines space–frequency code and MIMO OFDM-IM was proposed. It was shown that the presented scheme was capable of increasing the transmit diversity order.

5G and beyond networks using radio access virtualization strategies and advanced computational platforms will exploit network densification. The virtual cell concept removes the traditional cell boundary for the device and provides a consequent reduction in the detrimental "cell-edge experience" by the terminal. Traditionally, devices are associated with a cell and, as a consequence, the link performance may degrade as a terminal moves away from the cell center. In a virtualized cloud radio access network (C-RAN), the network determines which BSs or access points (APs) are to be associated with each terminal. The cell moves with the terminal in order to provide a cell-center experience throughout the entire network. Each terminal is served by its preferred set of APs. The actual serving set for a terminal may contain one or multiple BSs and the terminal's data are partially or fully available at some or a small set of potential serving BSs. The BS controller (central processor) will accommodate each terminal with its preferred set and transmission mode at every communication instance while considering load and channel state information (CSI) knowledge associated with the BS [27].

The 5G NR system [28–30] uses scalable OFDM numerology introducing specific subcarrier spacings (Δf), transmission time interval (TTI), cyclic prefix (CP) and the number of slots. Higher numerology indices correspond to larger subcarrier spacings (SCSs), ranging from 15 to 480 kHz according to the equation: $\Delta f = 15 \text{ kHz} \times 2^n$. The numerology index n depends on various factors (i.e., service requirements, deployment type, carrier frequency, etc.). The introduction of wider SCS is essential for mitigating inter-carrier interference (ICI) and phase noise at millimeter-wave (mmWave) frequencies. As SCS widens, the TTI assumes smaller values ranging from 1 ms to 31.25 µs. 5G NR was designed to lower interference and increase EE by reducing always-on transmissions, which is a crucial aspect to extend the lifetime of IoT devices. 5G NR ensures forward compatibility as it is prepared for its future 6G evolution in use cases and technologies. The introduction of mini-slots made 5G NR capable of guaranteeing low-latency requirements for ultrareliable and low-latency communication (URLLC). At mmWave frequencies, high capacity and extreme data rates are possible, even though higher frequencies introduce limitations in coverage due to increased signal attenuation [31]. 5G NR specifications are projected to accommodate dense urban scenarios, but with the introduction of mmWave, it can be more likely to have some part of the signal blocked by obstacles or severely affected by distance, which causes a substantial decrease in the signal strength, becoming hard to compensate even with advanced signal processing techniques [32,33].

Motivated by the work above, in this paper we study the adoption of precoding-aided transmitter-side generalized space–frequency IM (PT-GSFIM) as an alternative multiuser MIMO (MU-MIMO) scheme for the downlink in 5G and beyond systems. Besides exploiting both frequency and space domain resources through IM, different M-QAM constellation orders can be supported so as to accommodate flexible tradeoffs between SE, performance and complexity. In this paper we extend our previous work in [25], where we presented the design of a precoder and different detection algorithms for PT-GSFIM. The present scheme uses the same precoder to remove the MUI between BS and receivers, breaking the MU communication into equivalent small SU links and achieving a lower complexity at the receiver side. Furthermore, we adopt subcarrier-level interleaving combined with SSD

techniques as it allows the proposed approach to exploit the inherent diversity in frequency-selective channels and achieve improved performance without requiring additional power or bandwidth. In this paper, we focus on the system-level assessment of a C-RAN based on the PT-GSFIM scheme. The system-level evaluation is performed for numerologies 1 and 2 from 5G NR in three 3D scenarios with different parameters, such as modulation, number of transmitted antennas per user, bandwidth and frequency carrier, and it is benchmarked against two alternative MU-MIMO schemes. System-level simulations were performed based on PT-GSFIM link-level results between the BSs and the multiple terminals, where it is considered that the alternating direction method of multipliers (ADMM) detection algorithm from [25] is applied on the receiver side. System-level evaluation demonstrates that C-RAN deployments in several indoor and outdoor scenarios, including urban or mixed, can achieve significant performance and coverage improvements over typical cellular networks.

The paper is organized as follows: Section 2 presents the model for the PT-GSFIM system. Section 3 presents the transmitter and receiver structure as well as the different 5G NR scenarios that are considered in the evaluation. Section 4 presents and discusses the link- and system-level simulation results. The conclusions are outlined in Section 5.

Notation: Matrices and vectors are denoted by uppercase and lowercase boldface letters, respectively. $(.)^{\mathrm{T}}$ and $(.)^{\mathrm{H}}$ denote the transpose and conjugate transpose of a matrix/vector, $\| \cdot \|_p$ is the $\updownarrow_p$-norm of a vector, $\| \cdot \|_0$ is its cardinality, supp(**x**) returns the support of x, $\lfloor \cdot \rfloor$ is the floor function and $\boldsymbol{I}_n$ is the $n \times n$ identity matrix.

2. System Model

We consider the downlink of an OFDM-based MU-MIMO system, where a BS equipped with N_{tx} antennas transmits to N_u users. Each user is assumed to have N_{rx} antennas each, wherein that transmission is composed by grouping the subcarriers into N_f-sized subblocks, with only N_{af} of them active at any given moment, as seen in Figure 1.

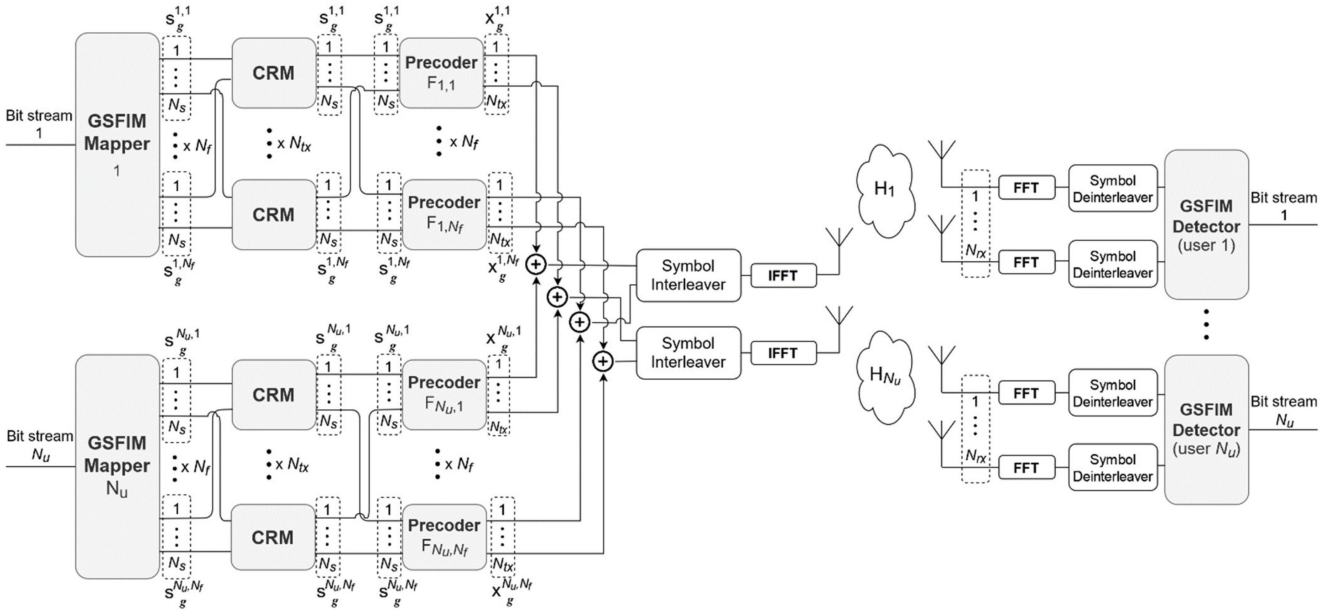

Figure 1. Transmitter and receiver structure [25].

As an example, if we have a scenario with $N_f = 8$ and $N_{af} = 6$, then only six out of each group of eight subcarriers are selected, and only the selected ones are activated to convey modulated symbols through their respective indices. This pattern of activation of subcarriers is also combined with the pattern of activation of the spatial domain which means that not all antennas will be transmitting in an active subcarrier. In fact, denoting N_s

as the total number of streams assigned to the antennas on each subcarrier, then only N_a of the position will contain modulated symbols which will correspond to active antennas.

2.1. Precoding-Aided Transmitter-Side Generalized Space–Frequency Index Modulation (PT-GSFIM)

We adopt an OFDM-based MU-MIMO as basis, where part of the information is mapped to conventional M-sized APM symbols and the remaining is encoded onto spatial and frequency indices. We assume a transmission block matrix where the bits are mapped in a simple way, with the encoding of the spatial indices executed independently from the frequency indices. In this case, simple look-up tables (LUTs) are inside each subblock: one for the spatial resources and another for the frequency resources. Although some SE is sacrificed when the mapping is done independently (the number of available space–frequency blocks that are indices is normally reduced), it simplifies the detection process as well the mapping/demapping process, as we will show further below. It is important to highlight that the approach based on a pair of LUTs is only adequate when a small number of both active antenna combinations and active subcarrier combinations exists. When this number is large, a different strategy can be employed, as described in [11,34].

Defining a PT-GSFIM symbol as $\mathbf{s}_g^u \in \mathbb{C}^{N_s N_f \times 1}$, for the u-th user, it can be written as $\mathbf{s}_g^u = \left[\left(\mathbf{s}_g^{u,1}\right)^T \cdots 0 \cdots \left(\mathbf{s}_g^{u,N_{af}}\right)^T \right]^T$, which corresponds to the concatenation of $(N_f$–$N_{af})$ length-N_s vectors of zeros with N_{af} GSM symbol vectors $\mathbf{s}_g^{u,i} \in \mathbb{C}^{N_s \times 1}$. These symbols are defined as $\mathbf{s}_g^{u,i} = \begin{bmatrix} 0 & s_{g,1}^{u,i} & 0 & \cdots & 0 & s_{g,N_a}^{u,i} & 0 \end{bmatrix}^T$, where $i = \left\{1, \cdots, N_{af}\right\}$, $u = \{1, \cdots, N_u\}$ and $g = \{1, \cdots, N_{GSFIM}\}$ (N_{GSFIM} is the number of PT-GSFIM symbols inside an OFDM block). Each of the N_{GSFIM} symbols is composed of all available antenna and subcarrier positions, where each is activated and deactivated according to their indices. The symbols $s_{g,j}^{u,i}$, where $j = \{1, \cdots, N_a\}$, are selected from an APM constellation. Since we are considering an MU downlink situation, where precoding is applied, the expression for the transmitted signal can be written as

$$\mathbf{x}_g = \sum_{u=1}^{N_u} \mathbf{F}_u \mathbf{s}_g^u = \mathbf{F}\mathbf{s}_g \tag{1}$$

where $\mathbf{s}_g = \left[\left(\mathbf{s}_g^1\right)^T \cdots \left(\mathbf{s}_g^{N_u}\right)^T \right]^T$ and $\mathbf{F} = [\mathbf{F}_1 \cdots \mathbf{F}_{N_u}]$, with $\mathbf{F}_u \in \mathbb{C}^{N_{tx} N_f \times N_s N_f}$ representing the precoder matrix. After the precoders and interleavers (which are explained further ahead), the frequency domain symbols are concatenated into N-sized blocks and converted to time domain through an inverse fast Fourier transform (IFFT). Before the transmission occurs, a CP with length greater than the delay spread of the channel is added to each block. It is important to observe that each PT-GSFIM symbol can carry a total of bits per user calculated through

$$N_{bits} = N_{af}\left(\left\lfloor \log_2 \binom{N_s}{N_a} \right\rfloor + N_a \log_2 M \right) + \left\lfloor \log_2 \binom{N_f}{N_{af}} \right\rfloor \tag{2}$$

where N_s is the number of available spatial positions on each subcarrier which is constrained to $N_s \leq N_{tx}/N_u$, and M is the size of the constellation adopted for the conventional modulated symbols.

2.2. 5G New Radio 3D Scenarios

There are several 5G test scenarios [35]. The three most important ones are described here and later evaluated using the multidimensional PT-GSFIM signals [25].

2.2.1. Urban Macro

The urban macro (UMa) homogeneous deployment scenario focuses on large cells and continuous coverage. This scenario will be interference-limited, using macro transmission

and reception points (TRPs, radio BSs above rooftop level). The intersite distance (ISD) in this scenario is 500 m, with the BS antenna height being 25 m. The carrier frequency is 3.5 GHz or 28 GHz. The bandwidth for 3.5 GHz and 28 GHz is up to 100 MHz and 1 GHz, respectively. Full buffer model is assumed. A total of 20 pieces of user equipment (UEs) are distributed per sector of each cell, with 80% of users being indoor with 3 km/h velocity and the remaining 20% being in cars with 30 km/h velocity. All parameters used correspond to the Table 7.2-1 in [36].

2.2.2. Urban Micro—Street Canyon

The urban micro (UMi) deployment scenario focuses on urban micro cells and high user densities and traffic loads in city centers and dense urban areas. This scenario will be interference-limited, using micro TRPs with micro cells. The ISD for the micro cells is 200 m. There are three micro cells per macro cell, with the micro-BS antenna height being 10 m. The carrier frequency and bandwidths for micro cells are the same as for urban macro cells. Full buffer traffic model is assumed. A total of 10 UEs are distributed per micro sector with 80% of users being indoor with a moving speed of 3 km/h and the remaining 20% being in cars with a velocity of 30 km/h. All parameters used correspond to the Table 7.2-1 in [36]. The layout of this scenario is illustrated on Figure 2.

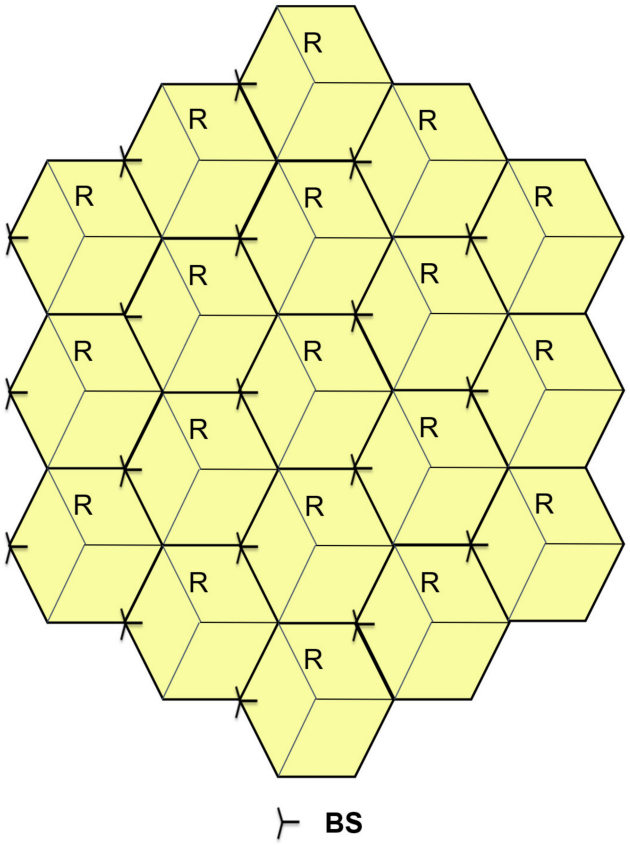

Figure 2. Urban micro scenario layout: Macro layer: ISD = 200 m = 3R; Micro layer: 3 micro TRPs per macro TRPs.

2.2.3. Indoor Hotspot

The indoor hotspot deployment scenario focuses on small coverage per cell and high user throughput or user density in buildings. This scenario represents indoor offices (InDs) with a total area of 120 m $\times$ 50 m. There are 12 small cells that are deployed with an ISD of 20 m. In this case, the BS antenna height is 3 m. The carrier frequency options are 30 and 70 GHz (mmWaves). The bandwidth for both 30 and 70 GHz carriers is up to 1 GHz. A total of 10 users per cell are distributed uniformly, and all users are indoors with 3 km/h

velocity. Full buffer model is assumed. The layout of this scenario is illustrated in Figure 3. All parameters used correspond to the Table 7.2-2 in [36].

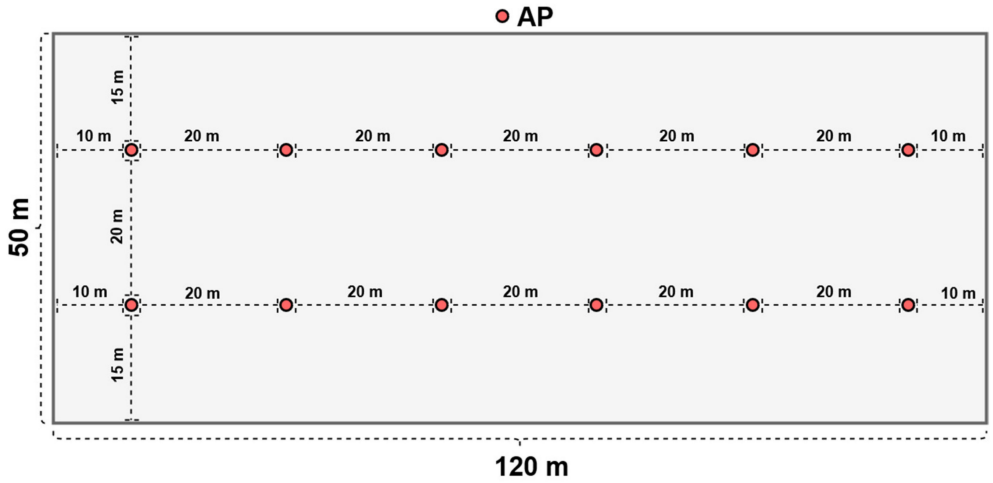

Figure 3. Indoor office scenario layout.

Our 3D simulation channel model considers the above-mentioned indoor and outdoor wireless propagation environments in terms of physical aspects of mmWave frequencies while numerous 5G NR channel models issues are adopted [36,37]. For any considered operating frequency and scenario, the number of clusters, the number of subarrays (scatterers) per cluster and the positions of the clusters can be determined by the detailed steps and procedures of [36,37]. According to the 5G 3GPP 3D channel models, the numbers of clusters and scatterers are determined using the Poisson and uniform distributions with specific parameters. Since 5G NR extends the operating frequency range by comprising the frequency bands below 7 GHz (i.e., FR1) and in the range from 24.25 to 52.6 GHz (i.e., FR2), different antenna solutions and techniques need to be employed depending on the utilized spectrum. For lower frequencies, up to a moderate number of antennas can be activated (i.e., 64). In higher frequency bands, the transmission is characterized by a considerable signal attenuation that limits the network coverage. To overcome this limitation, one of the key features is the adoption of a large number of multiantenna elements having a given aperture to increase the transmission/reception capability of MU-MIMO and beamforming. Since managing transmissions in higher frequency bands is complicated, beam management is necessary to establish the correspondence between the directions of the transmitter- and receiver-side beams by identifying the most suitable beam pair for both downlink and uplink.

3. Transmitter and Receiver Structure

In this section, we describe the transmitter and receiver structures adopted. Section 3.2 addresses the use of complex rotation matrices (CRMs) so as to integrate SSD into PT-GSFIM symbol design. The last subsection presents the adopted receiver algorithm.

3.1. Precoder Design

Assuming the time domain samples have been converted to the frequency domain through an N-point fast Fourier transform (FFT) and the CP has been discarded, the g-th PT-GSFIM symbol received by the user can be written as

$$\mathbf{y}_g^u = \mathbf{H}_g^u \mathbf{x}_g + \mathbf{n}_g^u = \mathbf{H}_g^u \mathbf{F}_u \mathbf{s}_g^u + \mathbf{H}_g^u \sum_{\substack{j=1 \\ j \neq u}}^{N_u} \mathbf{F}_j \mathbf{s}_g^j + \mathbf{n}_g^u \quad (3)$$

where $\mathbf{y}_g^u \in \mathbb{C}^{N_{rx}N_f \times 1}$, $\mathbf{n}_g^u \in \mathbb{C}^{N_{rx}N_f \times 1}$ represents the noise and $\mathbf{H}_g^u \in \mathbb{C}^{N_{rx}N_f \times N_{tx}N_f}$ is the frequency domain channel matrix between the BS and the user u. Since we are considering an OFDM scheme, the channel matrix follows a block diagonal structure and can be written as

$$\mathbf{H}_g^u = \text{blkdiag}\left\{\mathbf{H}_g^{u,1}, \cdots, \mathbf{H}_g^{u,f}, \cdots, \mathbf{H}_g^{u,N_f}\right\} \tag{4}$$

with $\mathbf{H}_g^{u,f} \in \mathbb{C}^{N_{rx} \times N_{tx}}$, $f = 1, \cdots, N_f$. As seen on the right side of (3), the second term represents the interference between users. Using the approach of block diagonalization (BD) described in [38] for the design of the precoder matrices $\mathbf{F}_u$, it is possible to eliminate all MUI from all the receivers. It is important to note that the signals conveyed on each subcarrier only generate interference on that subcarrier due to the block diagonal structure of $\mathbf{H}_g^u$. This means that the precoder matrices $\mathbf{F}_u$ for each subcarrier can be built independently and follow a block diagonal structure; i.e.,

$$\mathbf{F}_u = \text{blkdiag}\left\{\mathbf{F}_{u,1}, \cdots, \mathbf{F}_{u,N_f}\right\} \tag{5}$$

with $\mathbf{F}_{u,f} \in \mathbb{C}^{N_{tx} \times N_s}$, $f = 1, \cdots, N_f$. Each of the component precoder matrices $\mathbf{F}_{u,f}$ is generated so as to enforce $\mathbf{H}_g^{v,f}\mathbf{F}_{u,f} = 0$ for all $v \neq u$, canceling all MUI. Let us define the matrix that concatenates all the channel matrices between the base station and all users, except user u, for the subcarrier f as

$$\tilde{\mathbf{H}}_g^{u,f} = \left[\left(\mathbf{H}_g^{1,f}\right)^T \cdots \left(\mathbf{H}_g^{u-1,f}\right)^T \left(\mathbf{H}_g^{u+1,f}\right)^T \cdots \left(\mathbf{H}_g^{N_u,f}\right)^T\right]^T \tag{6}$$

This matrix models the transmission of the signal targeted at the u-th user when it reaches all of the other receivers, which causes interference, thus corresponding to the interference channel matrix. The appropriate precoder matrix $\mathbf{F}_{u,f}$ can be designed using an orthonormal basis of the null space of $\tilde{\mathbf{H}}_g^{u,f}$, starting from the singular value decomposition (SVD) of $\tilde{\mathbf{H}}_g^{u,f}$, which is given by

$$\tilde{\mathbf{H}}_g^{u,f} = \tilde{\mathbf{U}}_{u,f}\tilde{\mathbf{\Lambda}}_{u,f}\left[\tilde{\mathbf{V}}_{u,f}^{(1)}\ \tilde{\mathbf{V}}_{u,f}^{(0)}\right]^H \tag{7}$$

where $\tilde{\mathbf{U}}_{u,f}$ is the matrix with the left-singular vectors, $\tilde{\mathbf{\Lambda}}_{u,f}$ is a rectangular diagonal matrix with the decreasing nonzero singular values, $\tilde{\mathbf{V}}_{u,f}^{(1)}$ contains the right singular vectors corresponding to the nonzero singular values and $\tilde{\mathbf{V}}_{u,f}^{(0)}$ contains the remainder right singular vectors. To guarantee zero MUI in each precoder matrix, each precoder can be set as $\mathbf{F}_{u,f} = \tilde{\mathbf{V}}_{u,f}^{(0)}[:, 1 : N_s]$. In this case, at each receiver, the resulting signal is reduced to

$$\mathbf{y}_g^u = \hat{\mathbf{H}}_g^u \mathbf{s}_g^u + \mathbf{n}_g^u \tag{8}$$

where $\hat{\mathbf{H}}_g^u = \mathbf{H}_g^u\mathbf{F}_u$ is the equivalent SU channel. It can be observed that there is no presence of MUI in the resulting signal. Keeping in mind that both $\mathbf{H}_g^u$ and $\mathbf{F}_u$ have a block diagonal structure, $\hat{\mathbf{H}}_g^u$ will be block diagonal as well. Only a few positions of $\mathbf{s}_g^u$ will tend to be nonzero, according to the stated system model. As a result, $\mathbf{s}_g^u$ is a sparse vector, and its sparsity can be used to lower the transmitted power. To do this, we can use the same strategy that we considered in [39] for virtual GSM transmissions, in which an alternative signal is generated to reduce the transmitted power while assuring that the signals arriving at receivers are similar to the original ones. Although we assume fully digital precoders in

this paper, it is possible to simplify the implementation complexity of the proposed solution by using a hybrid precoder design comprising a reduced digital part and an analog part supported for example on analog phase shifters (and which are the same for all subcarriers). The hybrid design can be easily accomplished following the approximation-based approach described in [40].

3.2. Complex Rotation Matrices

A GSM symbol vector forming a PT-GSFIM is subject to the influence of the channel on a single subcarrier since, according to the signal model of Equation (8), $\hat{\mathbf{H}}_g^u$ is block diagonal. However, we can incorporate SSD techniques into the design of PT-GSFIM in order to take advantage of the inherent diversity of frequency-selective channels commonly seen in mobile propagation situations. SSD was first proposed in [41] and can be used to increase performance without requiring more power or bandwidth. In the proposed approach, we apply SSD by spreading each GSM symbol that makes up the primary PT-GSFIM symbol over different subcarriers through the use of CRMs. Working with a rotating super-symbol is part of the CRM application procedure. In this situation, we only apply the spreading in the frequency direction, which means that all of the spatial components are rotated simultaneously. For each user u, the rotated length-N_sN_f super-symbol can be expressed as

$$\breve{\mathbf{s}}_g^u = \left(A_{N_f} \otimes \mathbf{I}_{N_s}\right) \cdot \mathbf{s}_g^u \tag{9}$$

and the transmitted signal becomes (1)

$$\mathbf{x}_g = \sum_{u=1}^{N_u} \mathbf{F}_u \left(\mathbf{A}_{N_f} \otimes \mathbf{I}_{N_s}\right) \mathbf{s}_g^u = \mathbf{F}\left(\mathbf{I}_{N_u} \otimes \left(\mathbf{A}_{N_f} \otimes \mathbf{I}_{N_s}\right)\right) \mathbf{s}_g \tag{10}$$

Matrix $\mathbf{A}_{N_f} \in \mathbb{C}^{N_f \times N_f}$ can be chosen from the family of orthonormal complex matrices (OCRMs), which is defined as

$$\mathbf{A}_{M_{CRM}} = \begin{cases} \begin{bmatrix} e^{j\varphi} & je^{-j\varphi} \\ je^{j\varphi} & e^{-j\varphi} \end{bmatrix} / |\mathbf{A}_2|^{1/2}, M_{CRM} = 2 \\ |\mathbf{A}_2| = \det(\mathbf{A}_2) = 2 \\ \begin{bmatrix} \mathbf{A}_{M_{CRM}/2} & \mathbf{A}_{M_{CRM}/2} \\ \mathbf{A}_{M_{CRM}/2} & -\mathbf{A}_{M_{CRM}/2} \end{bmatrix} / |\mathbf{A}_{M_{CRM}}|^{1/M_{CRM}}, M_{CRM} > 2 \end{cases} \tag{11}$$

where $M_{CRM} = 2^n$, $|\mathbf{A}_{M_{CRM}}| = \det(\mathbf{A}_{M_{CRM}})$ and φ is the rotation angle [42]. To get the most out of frequency diversity, a subcarrier-wise interleaver is applied so that the effective group of subcarriers assigned to each PT-GSFIM symbol is spread out across the entire bandwidth. This interleaver is similar to the subcarrier-level block interleaver in [15]. However, in the case of PT-GSFIM, its effect is leveraged since with the use of CRMs, and each individual GSM symbol is spread over the different subcarriers allocated to the corresponding PT-GSFIM subblock.

3.3. Receiver Design

In the previous section, the transmitter side was described, where the use of a precoder removes all MUI from the receiver side. This means that only SU detection needs to be implemented at the receivers.

Due to the use of CRMs, each GSM symbol comprising a PT-GSFIM block is dispersed across numerous subcarriers. As a consequence, the received signal can be written as

$$\begin{aligned} \mathbf{y}_g^u &= \hat{\mathbf{H}}_g^u \breve{\mathbf{s}}_g^u + \mathbf{n}_g^u \\ &= \breve{\mathbf{H}}_g^u \mathbf{s}_g^u + \mathbf{n}_g^u \end{aligned} \tag{12}$$

where $\overset{\smile}{\mathbf{H}}_g^u = \overset{\wedge}{\mathbf{H}}_g^u \left(A_{N_f} \otimes \mathbf{I}_{N_s} \right)$ is the overall equivalent channel that the user u "perceives" for the g^{th}PT-GSFIM symbol. To design the detector, first, we formulate the maximum likelihood detection (MLD) problem as

$$\min_{\mathbf{s}_g^u} f(\mathbf{s}) \triangleq \left\| \mathbf{y}_g^u - \overset{\smile}{\mathbf{H}}_g^u \mathbf{s}_g^u \right\|_2^2 \tag{13}$$

$$\text{subject to } \mathbf{s}_g^u \in {\mathcal{A}_0}^{N_s N_f} \tag{14}$$

$$\text{supp}\left(\mathbf{s}_g^{u,i} \right) \in \mathbb{S}_0, i = 1, \ldots, N_f \tag{15}$$

$$\text{supp}\left(\mathbf{s}_g^u \right) \in \mathbb{J} \tag{16}$$

where $\mathcal{A}_0$ represents the set with the complex-valued symbols from the adopted APM constellation, including symbol 0. $\mathbb{S}_0$ denotes the set of valid supports of $\mathbf{s}_g^{u,i}$, according to the possible GSM symbols. $\mathbb{J}$ represents the set of valid supports of $\mathbf{s}_g^{u,i}$ according to all possible active subcarrier combinations. Applying the alternating direction method of multipliers (ADMM), following the approach described in [43], results in the algorithm in Table 1 In the algorithm, $\bar{I}$ designates the complement of the support set I and Q is the number maximum of iterations.

Table 1. Algorithm based in ADMM used for GSFIM detection [25].

Input: $\mathbf{x}^0$, $\mathbf{r}^0$, $\mathbf{z}^0$, $\mathbf{u}^0$, $\mathbf{v}^0$, $\mathbf{w}^0$, $\overset{\smile}{\mathbf{H}}_g^u$, $\mathbf{y}_g^u$, ρ_x, ρ_r, ρ_z, Q
$f_{best} = \infty$
$\mathbf{\Phi} \leftarrow \left(\left(\overset{\smile}{\mathbf{H}}_g^u \right)^H \overset{\smile}{\mathbf{H}}_g^u + (\rho_x + \rho_r + \rho_z) \mathbf{I}_{N_f N_s} \right)^{-1}$
for $t = 0, 1, \ldots Q$-1 **do**
$\mathbf{s}^{(t+1)} \leftarrow \mathbf{\Phi} \left(\left(\overset{\smile}{\mathbf{H}}_g^u \right)^H \mathbf{y}_g^u + \rho_x \left(\mathbf{x}^{(t)} - \mathbf{u}^{(t)} \right) + \rho_r \left(\mathbf{r}^{(t)} - \mathbf{v}^{(t)} \right) + \rho_z \left(\mathbf{z}^{(t)} - \mathbf{w}^{(t)} \right) \right)$
$\left(\mathbf{x}^i \right)^{(t+1)} \leftarrow \prod_{\mathbb{S}_0} \left(\left(\mathbf{s}^i \right)^{(t+1)} + \left(\mathbf{u}^i \right)^{(t+1)} \right)$
$\mathbf{r}^{(t+1)} \leftarrow \prod_{\mathbb{J}} \left(\mathbf{s}^{(t+1)} + \mathbf{v}^{(t)} \right)$
$\mathbf{z}^{(t+1)} \leftarrow \prod_{{\mathcal{A}_0}^{N_s N_f}} \left(\mathbf{s}^{(t+1)} + \mathbf{w}^{(t)} \right)$
$I \leftarrow \text{supp}\left(\mathbf{x}^{(t+1)} \right) \cap \text{supp}\left(\mathbf{r}^{(t+1)} \right)$
If $t = Q$-1 **then**
$\overset{\sim}{\mathbf{s}}_g^u[\bar{I}] \leftarrow 0$
$\overset{\sim}{\mathbf{s}}_g^u[I] \leftarrow \prod_{\mathcal{A}^{N_{af} N_a}} \left(\left(\left(\overset{\smile}{\mathbf{H}}_g^u[:, I] \right)^H \overset{\smile}{\mathbf{H}}_g^u[:, I] + 2\sigma^2 \mathbf{I}_{N_{af} N_s} \right)^{-1} \times \left(\overset{\smile}{\mathbf{H}}_g^u[:, I] \right)^H \mathbf{y}_g^u \right)$
else
$\overset{\sim}{\mathbf{s}}_g^u[\bar{I}] \leftarrow 0, \overset{\sim}{\mathbf{s}}_g^u[I] \leftarrow \mathbf{z}^{(t+1)}[I]$
end if
If $f\left(\overset{\sim}{\mathbf{s}}_g^u \right) < f_{best}$ **then**
$\overset{\wedge}{\mathbf{s}}_g^u[\bar{I}] \leftarrow 0$, $\overset{\wedge}{\mathbf{s}}_g^u[I] \leftarrow \overset{\sim}{\mathbf{s}}_g^u[I]$
$f_{best} = f\left(\overset{\sim}{\mathbf{s}}_g^u \right)$
end if
$\mathbf{u}^{(t+1)} \leftarrow \mathbf{u}^{(t)} + \mathbf{s}^{(t+1)} - \mathbf{x}^{(t+1)}$
$\mathbf{v}^{(t+1)} \leftarrow \mathbf{v}^{(t)} + \mathbf{s}^{(t+1)} - \mathbf{r}^{(t+1)}$
$\mathbf{w}^{(t+1)} \leftarrow \mathbf{w}^{(t)} + \mathbf{s}^{(t+1)} - \mathbf{z}^{(t+1)}$
end for
Output: $\overset{\wedge}{\mathbf{s}}_g^u$

In line 6, $\prod_{\mathbb{S}_0}(\cdot)$ denotes the projection over $\mathbb{S}_0$ which can be completed by choosing the N_a largest magnitude elements, and whose indices also correspond to a valid active antenna combination. If set $\mathbb{S}_0$ is very large, the projection can be simplified to a basic cardinality-based one. In this situation, the projection can be obtained by turning to zeros the N_s–N_a smallest magnitude elements. Step 7 requires computing the projection over set $\mathbb{J}$, $\prod_{\mathbb{J}}(\cdot)$, which may be achieved by nulling all, except the N_{af} columns of the matrix $\mathbf{R} = vec^{-1}_{N_s \times N_f}\left(\mathbf{s}^{(t+1)} + \mathbf{v}^{(t)}\right)$ which have a higher Euclidean norm and which also match a valid active subcarrier combination. If set $\mathbb{J}$ is very large, the projection can also be simplified to a basic cardinality-based projection. In this case, we simply need to zero the N_f–N_a columns of $\mathbf{R}$ with a smaller Euclidean norm. Step 8 involves a projection over set ${\mathcal{A}_0}^{N_s N_f}$, $\prod_{{\mathcal{A}_0}^{N_s N_f}}(\cdot)$, which can be computed elementwise through simple rounding to the nearest element in $\mathcal{A}_0$. The projection in step 11 can be performed in a similar way.

4. Numerical Results

In this section, we present numerical simulations, both link- and system-level, for the PT-GSFIM-based downlink scheme integrated into a 5G NR system. Results are presented in bit error rate (BER) and measure the performance of the signal across the entire communication chain, from transmitter to receiver. Link performance results, namely block error rate (BLER) results, are used as input by the system-level simulator. We consider a virtualized C-RAN, where the network determines which BSs or APs are to be associated with each terminal. The total number of BSs or APs depends on the scenario and are indicated in Tables 1 and 2. Each BS or AP consists of three TRPs, each one equipped with N_{tx} antennas, while users have N_{rx} antennas. The BS or AP array configuration corresponds to three uniform linear arrays, each with 256 antennas, where the separation between antennas of the array is half-wavelength [44]. The system-level block diagram can be found in [36,37,45,46].

4.1. Link-Level Simulations

In this section, the performance of the proposed PT-GSFIM scheme is assessed and compared against other MU-MIMO systems. Monte Carlo simulations were run according to the system model presented previously.

Figure 4 shows a comparison of block diagonalization (BD)-based MU-MIMO scheme from [38], GSM MU-MIMO from [39] and the PT-GSFIM from [25]. We assume a scenario with N_u = 8, N_a = 2 and N_{rx} = 5 for all schemes, while keeping the same SE, close to 12 bits per channel use (bpcu). SE is computed through Equation (2), divided by N_f. We also employ a total of $N_{tx} = 12N_u$ antennas for all three schemes, with PT-GSFIM and BD MU-MIMO using the ADMM algorithm for the detection and GSM using the OB-MMSE algorithm from [47]. The CRM adopted in the PT-GSFIM scheme considers a rotation angle φ of 30°. Both GSM and PT-GSFIM are using a 16QAM constellation, whereas 64QAM is used in BD MU-MIMO. To ensure a fair comparison, all schemes have an SE close to 12 bpcu per user. It can be observed that the PT-GSFIM scheme outperforms both GSM and traditional MU-MIMO, and the gains are greater when the symbols are distributed over a larger number of subcarriers (N_f). At the end of the paper, we will compare these three MU-MIMO schemes based on system-level simulations.

A second set of simulations were performed in order to analyze the BLER performance versus the energy per symbol to noise power spectral density (E_s/N_0) in dB for the proposed PT-GSFIM system. For these BLER simulations, a minimum of 25,000 blocks were transmitted for computing each BLER result.

In Figure 5, BLER is presented versus (E_s/N_0) in dB for three cases of M-QAM modulations, namely $M \in \{4,16,64\}$. We have different SEs for 64QAM, namely 12.5 bpcu and 11.75 bpcu; for 16QAM, the SE is 11.9375 bpcu; and for 4QAM (QPSK), we have 6.5 bpcu and 5.75 bpcu. The difference between them is the number of transmitting antennas per user, which was 8 antennas per user for 64QAM (12.5 bpcu) and 4QAM (6.5 bpcu), 5 antennas per user for 64QAM (11.75 bpcu) and 4QAM (5.75 bpcu) and 12 antennas per user are

used for 16QAM (11.9375 bpcu). As expected, higher values of M require higher values of E_s/N_0 to reach the reference BLER = 10^{-1}. A higher number of antennas per user increases the bpcu and decreases the E_s/N_0 required to reach the reference BLER.

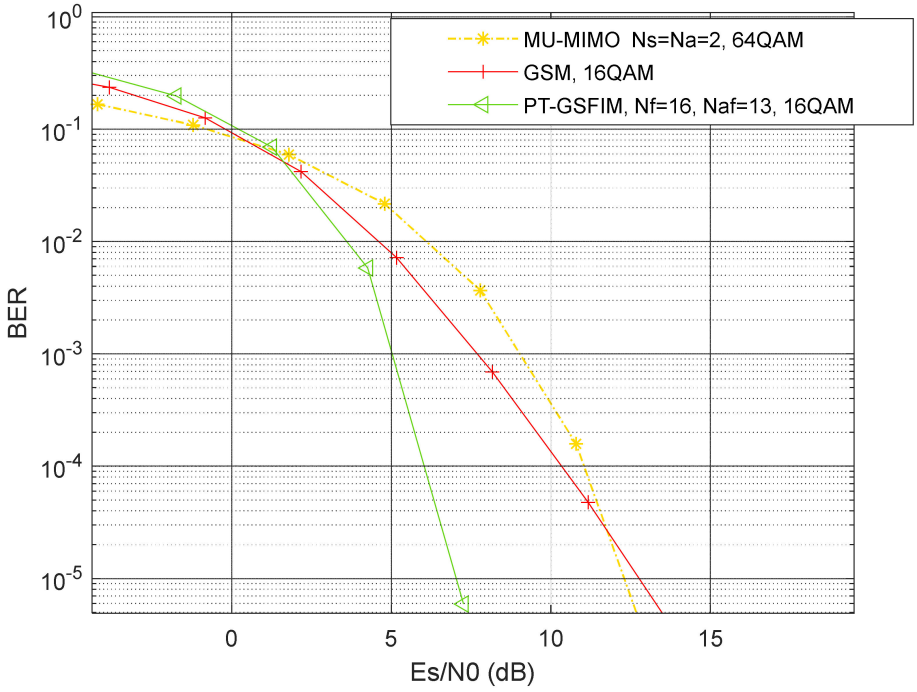

Figure 4. Comparison of BER performances of PT-GSFIM, GSM and conventional BD MU-MIMO, with N_u = 8 and SE = 12 bpcu.

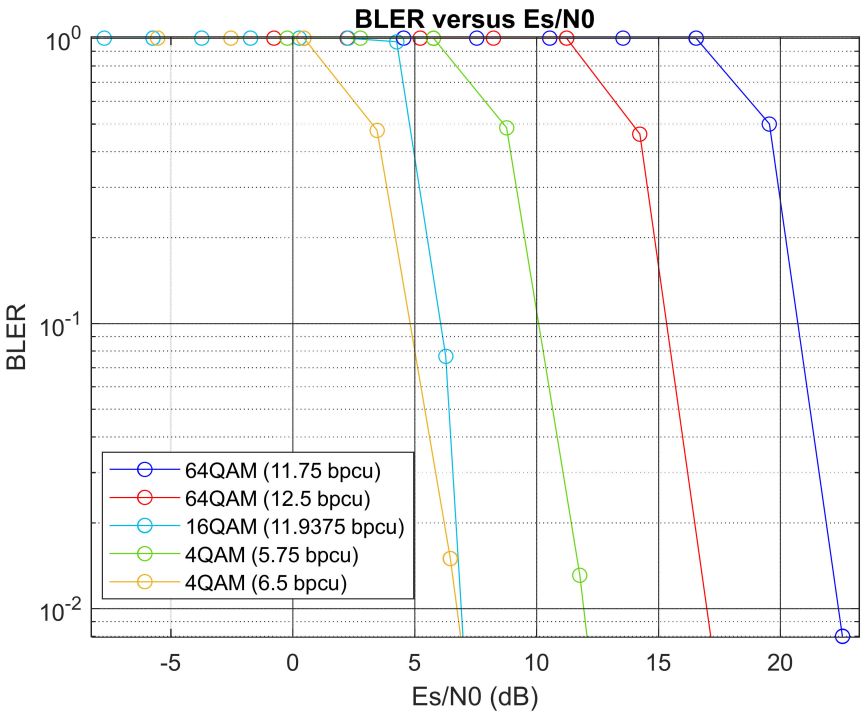

Figure 5. BLER vs. (E_s/N_0) dB curves for PT-GSFIM in an MU scenario with N_{rx} = 5, 64QAM (11.75 bpcu and 12.5 bpcu), 16QAM (11.9375 bpcu) and 4QAM (5.75 and 6.5 bpcu).

4.2. System-Level Simulations

Using the PT-GSFIM link-level results, in this subsection we describe several system-level simulations that were performed for a C-RAN incorporating PT-GSFIM, considering different scenarios and 5G NR numerologies. The signal-to-noise ratio (SNR) in dB considered in the system-level simulations is obtained from $SNR = (E_s/N_0) + 10\ log(Rs/B)$ dB, where Rs is the total transmitted symbol rate per antenna and user, B is the total bandwidth (we considered 20 MHz at 3.5 GHz and 50 MHz at 28 GHz) and E_s/N_0 is the ratio of symbol energy to noise spectral density in dB. Values of E_s/N_0 are obtained from the link-level BLER results. 5G NR frame structure has both frequency division duplex (FDD), used in the paired spectrum, and time division duplex (TDD), used for the unpaired spectrum. We chose TDD in this work and 5G NR numerology 1 for UMi and UMa scenarios at 3.5 GHz and numerology 2 for InD scenario at 28 GHz [44]. For UMi and UMa scenarios, B = 20 MHz with normal CP, where the subcarrier spacing is 30 kHz and 28 OFDM symbols are transmitted in every subframe of 1 ms. For InD scenario, B = 50 MHz, the subcarrier spacing is 60 kHz and 28 OFDM symbols are transmitted in every subframe of 0.5 ms. Other simulator parameters are as follows: maximum TRP transmit power of 49 dBm for UMa, 44 dBm for UMi and 30 dBm for InD, receiver spectral noise power density -174 dBm/Hz, CP overhead 5%, pilots/TRP = 50 and uniform linear arrays with uni-polarized antennas. Each user feedbacks all CSI and signal-to-interference-plus-noise ratio (SINR) to TRPs during uplink time slots. Equal duration of downlink and uplink time slots is assumed. Users are placed uniformly around TRPs and random waypoint mobility around TRPs is employed. We must consider that the full buffer is used. The static clustering technique partitions the network into three adjacent TRP sets where each user is served by at least one TRP, while the others perform inter-user interference. When C-RAN cluster size is one it means that there is no C-RAN BS clustering; this is the traditional cellular system. The UMi street canyon scenario is a high-density urban one where 80% of users are inside buildings and 20% of users are in the streets (such as UMa). However, the intersite distance is 200 m, which allows decreasing the total transmitted power from 49 dBm (UMa) to 44 dBm. Scenarios UMa and UMi street canyon can be directly compared because they both use numerology 1 and the same carrier frequency (3.5 GHz) and bandwidth B = 20 MHz. However, the scenario InD cannot be directly compared with the others because it uses numerology 2 with double the transmitted symbols per 1 ms, having a different bandwidth, B = 50 MHz, and a carrier frequency of 28 GHz.

Based on the parameters of Figure 6, and noting that we considered N_u = 50, 5 transmit antennas per user $N_{tx} = 5N_u$ and N_{rx} = 5 receive antennas per user, there are a total of 250 active antennas at each sector (one TRP per sector). 64QAM requires a higher SNR compared to 4QAM. InD is expected to offer the highest throughput due to its smaller size. This occurs independently of the modulation. UMi scenario assures the next best throughput performance, whereas UMa is the scenario with the lowest throughput. It is observed that the highest throughput performance is for InD with 4QAM-modulated packets. This is due to the InD scenario having twice the bit rate compared to the other scenarios. Moreover, InD has strong inter-interference and high propagation losses; however, most of the 4QAM packets are received correctly due to its required SINR being small. By contrast, most of the 64QAM packets are received with error because of its required SINR being high, resulting in lower average throughput. In other words, 64QAM packets are only correctly received close to the BS, while 4QAM packets are correctly received almost everywhere. Scenario UMi also has strong inter-interference between sites, and there is additional outdoor-to-indoor propagation loss for users that are inside the buildings. The throughput performance of 64QAM packets is lower than that of 4QAM packets in all scenarios. The explanation for this is the same given for the InD scenario. Scenario UMa also has strong inter-interference between sites, and due to the highest ISD, users at the cell borders suffer the smallest SINR. It also has additional outdoor-to-indoor propagation loss for users that are inside the buildings. As a consequence, the throughput performance of

UMa is the worst of the three scenarios. In UMa, the throughput performance of 4QAM packets is slightly higher than that of 64QAM packets.

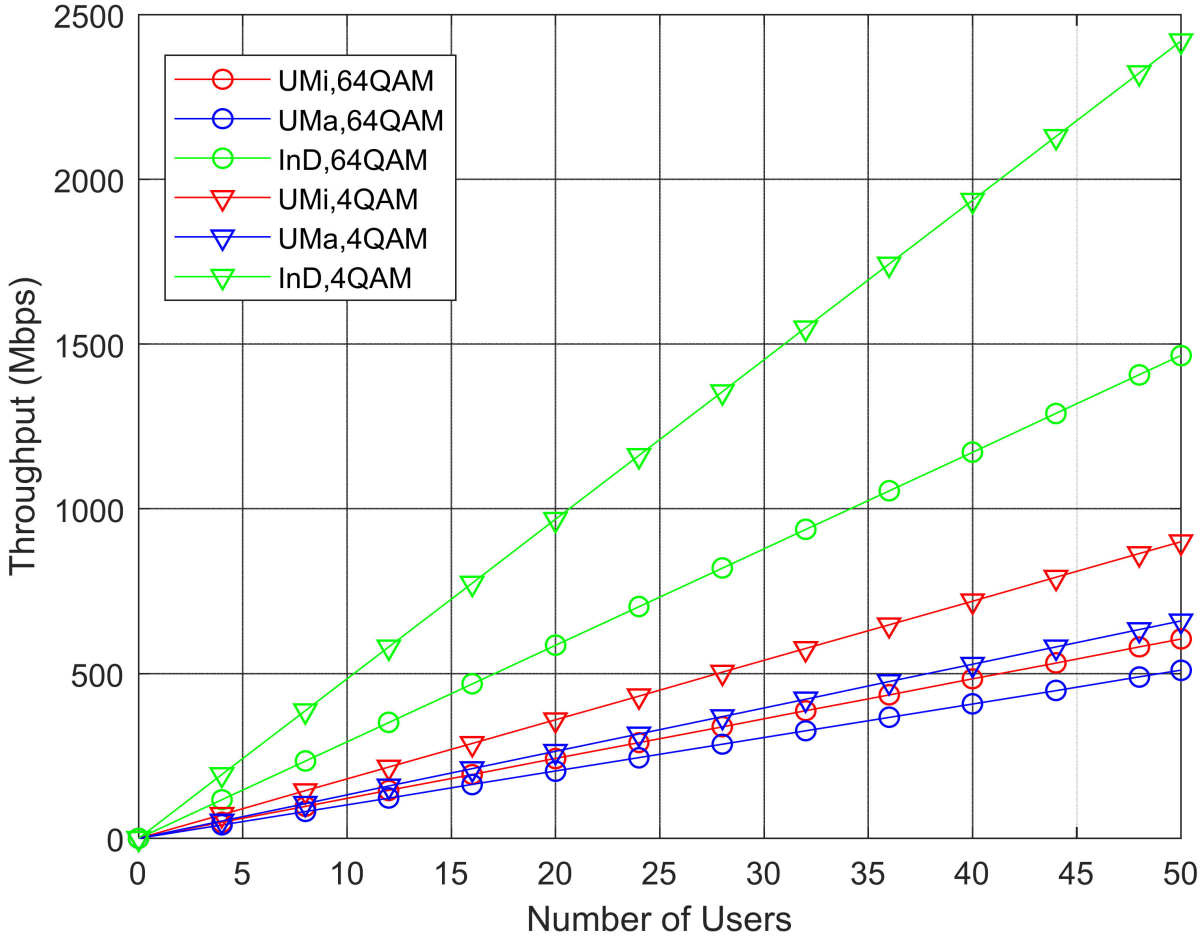

Figure 6. Throughput vs. number of users for different scenarios with $N_{tx} = 5N_u$, $N_f = 4$, $N_{af} = 3$, $N_s = 5$, $N_a = 2$, $N_{rx} = 5$, 64-QAM (11.75 bpcu per user) and 4QAM (5.75 bpcu per user), C-RAN cluster size 1.

In Figure 7, the RAN cluster size is 3, so the network is partitioned into three adjacent site sets and each user is served at the same time by three sites (generating much less inter-interference). The same maximum $N_u = 50$ from the previous scenario is also considered. From the comparison between Figures 6 and 7, it is clear that there is an improved throughput for clusters of three sites, due to much lower inter-interference between sites, especially for 64QAM in all scenarios. InD continues to offer the highest throughput due to its smaller size and double transmitted bit rate when compared to the other scenarios. The average throughput gain due to cluster size 3 for UMi is 4.6 for 64QAM and 2.0 for 4QAM. The gain for UMa is 3.9 for 64QAM and 2.7 for 4QAM. The gain for InD is 2.6 for 64QAM and 1.6 for 4QAM. For 4QAM (5.75 bpcu), the increase in throughput between 3C and 1C is less obvious due to its lower SE allowing higher cell coverage. For 50 users in UMi with 3C, the total throughput of 64QAM is 2.760 Gbps, which corresponds to a sector SE of 138 bps/Hz that is equivalent to almost 2.8 bps/Hz per user. For 50 users in InD, the total throughput of 64QAM is 3.875 Gbps, which corresponds to a sector SE of 77.5 bps/Hz that is equivalent to 1.55 bps/Hz per user. This is in agreement with higher frequency bands (28 GHz) which imply higher bandwidths (50 MHz) but lower SE, while lower frequency bands (3.5 GHz) result in lower bandwidths (20 MHz) but higher SE.

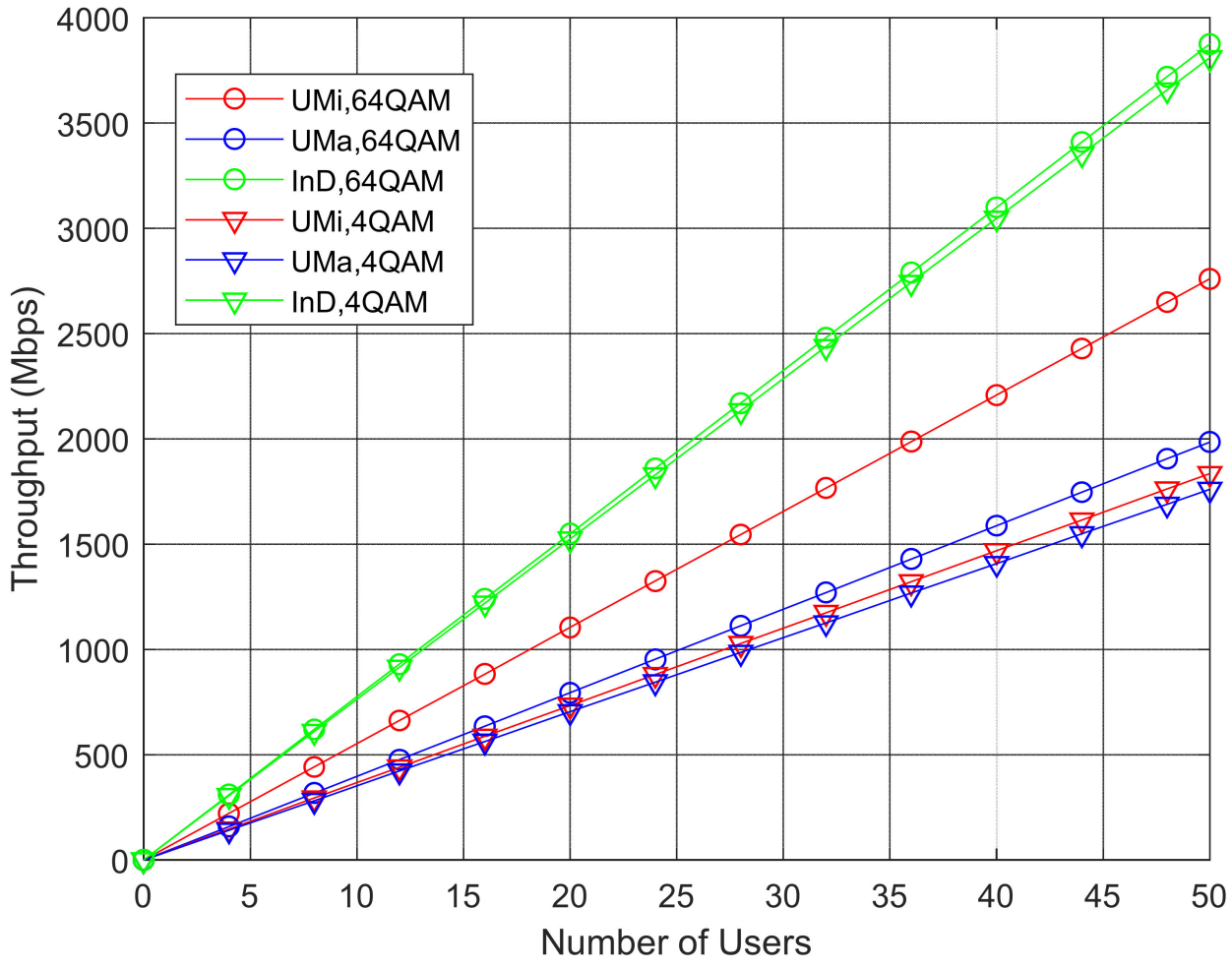

Figure 7. Throughput vs. number of users for different scenarios with $N_{tx} = 5N_u$, $N_f = 4$, $N_{af} = 3$, $N_s = 5$, $N_a = 2$, $N_{rx} = 5$, 64-QAM (11.75 bpcu per user) and 4QAM (5.75 bpcu per user), C-RAN cluster size 3.

Figure 8 presents the cumulative distribution function (CDF) of each user served by one TRP of the UMa scenario, based on the throughput results presented in Figures 6 and 7. This CDF statistic is based on the throughput per user achieved as a function of the distance between terminals and serving TRPs. Each TRP has $N_{tx} = 250$ active antennas serving 50 users each with $N_{rx} = 5$ antennas. We consider the C-RAN UMa scenario with two different cluster sizes, namely a cluster of size 1 (1C) and a cluster of size 3 (3C). As expected, only for 3C there is a percentage of users that achieve the maximum throughput. With 3C, not only users that are close to the TRPs are able to get the maximum throughput. About 20% of users for 64QAM and 50% of users for 4QAM are in this situation of achieving maximum throughput. For 4QAM with 1C, only users that are located quite close to the TRP antenna (less than 1%) are able to get maximum throughput. For 64QAM with 1C, no user is able to get the maximum throughput due to high inter-interference. For 4QAM with 1C, only users that are located quite close to the TRP antenna (less than 1%) are able to get maximum throughput. For 64QAM with 1C, no user is able to get the maximum throughput due to high inter-interference. So, for 64QAM, most of the packets are not received correctly, while for 4QAM, many of the packets are correctly received.

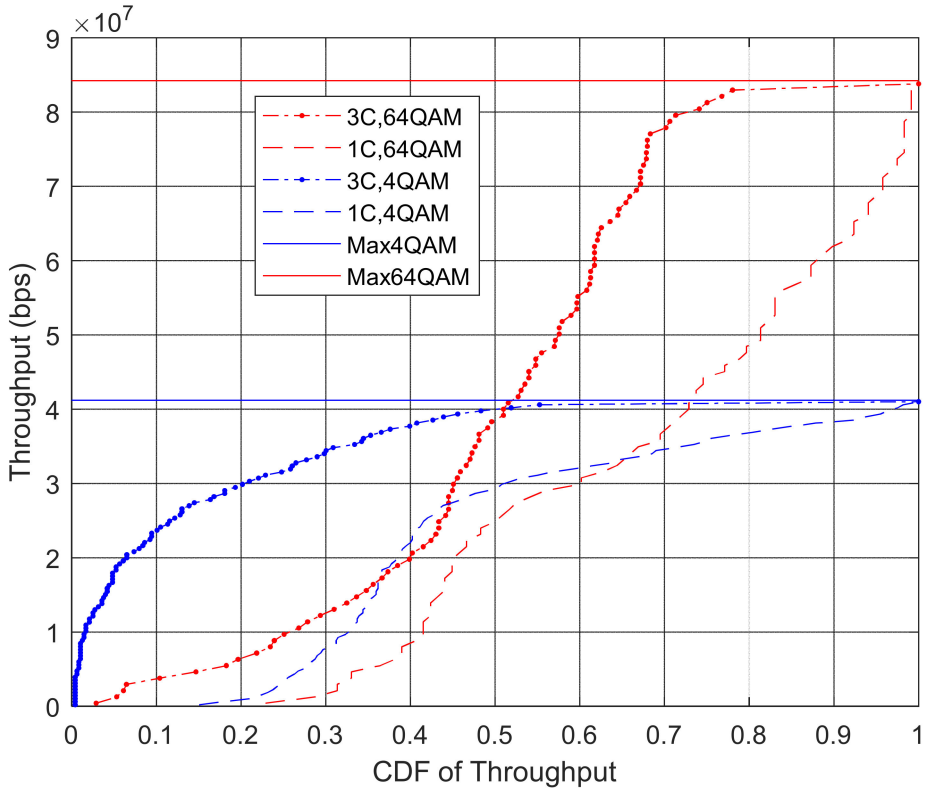

Figure 8. Throughput performance (bps) vs. CDF of throughput for UMa scenario with $N_{tx} = 5N_u$, $N_f = 4$, $N_{af} = 3$, $N_s = 5$, $N_a = 2$, $N_{rx} = 5$, 64QAM (11.75 bpcu per user) and 4QAM (5.75 bpcu per user).

Figure 9 presents the CDF of a TRP for the UMa scenario serving 20 users, during the simulation run with a duration of 100 s. These statistics are based on the throughput performance of each one of all users measured at each TTI = 0.5 ms during the simulation run. When we compare the maximum throughput values of Figures 8 and 9, we can see an increase of 14 for 4QAM and 7 for 64QAM. These numbers refer to 3C RAN clustering, confirming its lower inter-interference. In Figure 9, we can also observe the difference of 3 times more throughput achieved by RAN clustering 3C compared to the case of 1C. This occurs independently of the modulation. For 3C, there is a slight throughput gain of 64QAM-modulated packets compared to 4QAM packets. For 1C, there is a slight throughput gain of 4QAM packets compared to 64QAM. This corroborates the results of Figures 6 and 7, for the value of $N_u = 20$.

In Figure 10, we only consider the UMa scenario, we compare the throughput for three cases of the number of transmitting antennas per user N_{tx}/N_u, with RAN cluster sizes of 1 and 3. Based on the BLER results of Figure 5, the best BLER performance with the highest bpcu per user belongs to $N_{tx}/N_u = 12$, followed by $N_{tx}/N_u = 8$ and $N_{tx}/N_u = 5$. However, a higher number of transmitting antennas per user implies that a lower number of users are served, because the total number of TRP antennas is fixed and equals 256. The number of receiving antennas per user is kept fixed and equals 5. It should be pointed out that it is not clear what N_{tx}/N_u would provide higher throughput. From Figure 8, we conclude that the best N_{tx}/N_u ratio depends on the RAN cluster size and modulation. For cluster size 1, the highest throughput performance is for $N_{tx}/N_u = 12$ using 16QAM, and the lowest throughput is for 64QAM with $N_{tx}/N_u = 5$.

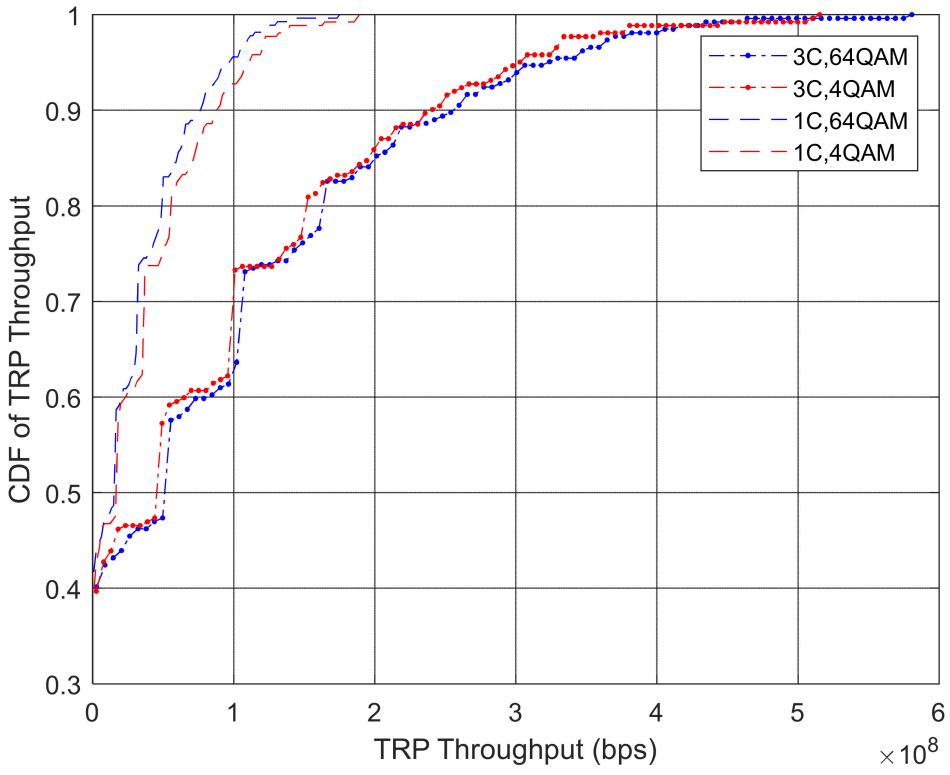

Figure 9. CDF of TRP throughput vs. TRP throughput (bps) for UMa scenario with $N_{tx} = 5N_u$, $N_f = 4$, $N_{af} = 3$, $N_s = 5$, $N_a = 2$, $N_{rx} = 5$, 64-QAM (11.75 bpcu per user) and 4QAM (5.75 bpcu per user).

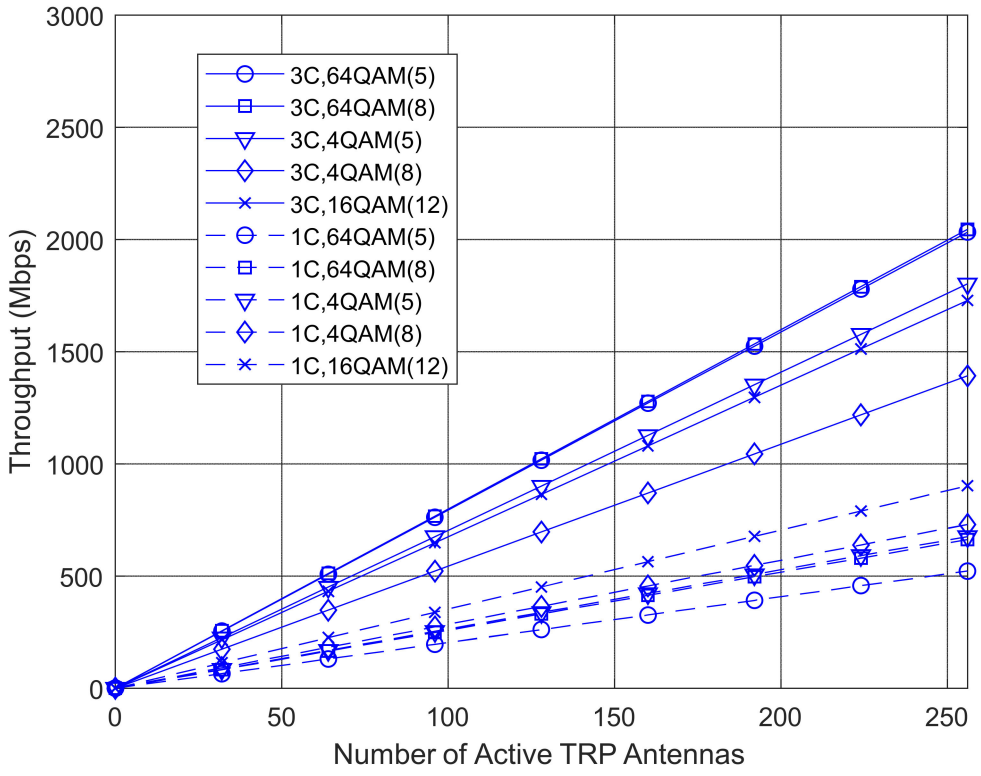

Figure 10. Throughput vs. number of active TRP antennas, for UMa scenario, $N_{rx} = 5$, for two C-RAN cluster sizes, modulations and numbers of antennas per user, namely with $N_{tx}/N_u = 5$, 64QAM(5) and 4QAM(5); with $N_{tx}/N_u = 8$, 64QAM(8) and 4QAM(8); and with $N_{tx}/N_u = 12$, 16QAM(12).

This result can be explained by the existence of high inter-interference in this cluster size, which affects mostly high-order modulations with the maximum number of users served at the same time. The case with N_{tx}/N_u = 12 using a constellation of 16QAM has the minimum number of users served at the same time but has the highest bpcu per user, resulting in the lowest interference, which is the best case. However, for cluster size 3, there is much less inter-interference between sites. In this case, the highest throughput performance is achieved for the two 64QAM cases, namely with N_{tx}/N_u = 8 or N_{tx}/N_u = 5. The lowest throughput is achieved for N_{tx}/N_u = 8 using 4QAM. This is explained by the low-order modulation and bpcu associated with a limited number of served users compared to the case of N_{tx}/N_u = 5. With a small level of inter-interference of cluster size 3, high-order modulations present the best throughput performance. From these results, we conclude that there is an optimum N_{tx}/N_u to achieve the highest throughput, but it depends on the cluster size and modulation. Higher N_{tx}/N_u with 16QAM is recommended for C-RAN cluster size 1 with a high level of inter-interference and a lower number of users per site. Lower N_{tx}/N_u with 64QAM is recommended for RAN cluster size 3 with lower inter-interference but a higher number of users per site.

Figure 11 corresponds to Figure 10, but in this case, we consider the UMi scenario. When we compare both figures, it is obvious that the best throughput performance is achieved in the UMi scenario. This was expected due to lower ISD, in spite of a higher number of users per unit of area. The total number of TRP antennas is the same and equals 256. The number of receiving antennas per user is kept fixed and equals 5. It is interesting to find the N_{tx}/N_u that provides higher throughput. From Figure 11, we can conclude that the best N_{tx}/N_u depends on the C-RAN cluster size and modulation. For cluster size 1, the highest throughput performance is obtained for N_{tx}/N_u = 12 using 16QAM, and the lowest throughput is achieved for 64QAM with N_{tx}/N_u = 5. The high inter-interference of this cluster size makes high-order modulation with the maximum number of users served at the same time the worst case of achieved throughput. The case N_{tx}/N_u = 12 using 16QAM has the minimum number of users served simultaneously but with the highest bpcu per user and continues to present the lowest interference, corresponding to the best case. Cluster size 3 has much less inter-interference between sites. In this case, the highest throughput performance is achieved for 64QAM with N_{tx}/N_u = 5.

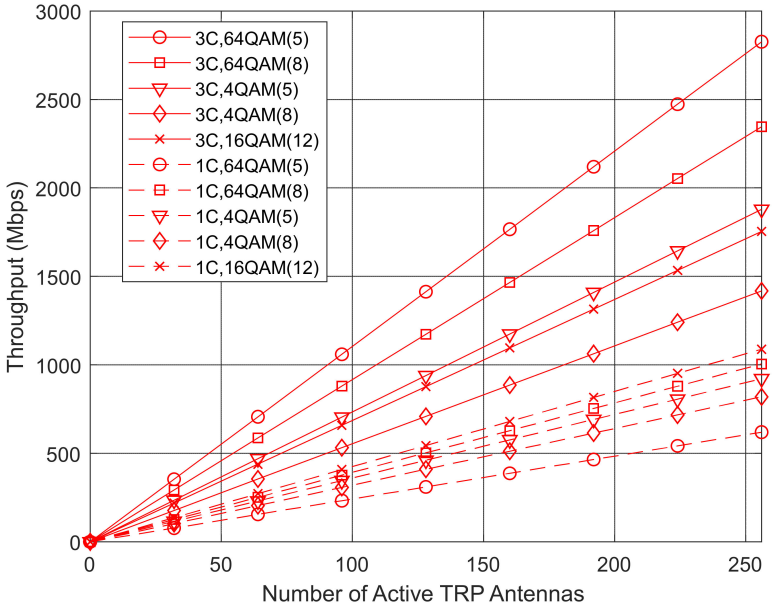

Figure 11. Throughput vs. number of active TRP antennas, for UMi scenario, N_{rx} = 5, for two C-RAN cluster sizes, modulations and numbers of antennas per user, namely with N_{tx}/N_u = 5, 64QAM(5) and 4QAM(5); with N_{tx}/N_u = 8, 64QAM(8) and 4QAM(8); and with N_{tx}/N_u = 12, 16QAM(12).

The lowest throughput is achieved for $N_{tx}/N_u = 8$ using 4QAM. This is explained by the low-order modulation and bpcu associated with a reduced number of served users compared to the case of $N_{tx}/N_u = 5$. Cluster size 3 has a small level of inter-interference, which allows the case of 64QAM with $N_{tx}/N_u = 5$ to achieve higher throughput than 64QAM with $N_{tx}/N_u = 8$ due to a higher number of users with almost the same bpcu. Considering what we have been observing throughout this study, we conclude that there is a value of N_{tx}/N_u that can achieve the highest throughput, but it depends on the cluster size and modulation. Higher N_{tx}/N_u with 16QAM is recommended for C-RAN cluster size 1 with a high level of inter-interference and a lower number of users per site. 64QAM with $N_{tx}/N_u = 5$ is recommended for C-RAN cluster size 3 with lower inter-interference but a higher number of users per site.

Figure 12 corresponds to Figures 10 and 11, but in this case, we consider the InD scenario. When we compare the three figures, it is obvious that the best throughput performance is attained in the InD scenario. This was expected due to the 2-fold increase in the transmitted bit rate and lower ISD, in spite of the highest number of users per unit of area. The total number of TRP antennas is the same and equals 256. The number of receiving antennas per user is kept fixed and equals 5. In this case, we also wanted to find the value of N_{tx}/N_u that could provide the highest throughput in this InD scenario at 28 GHz.

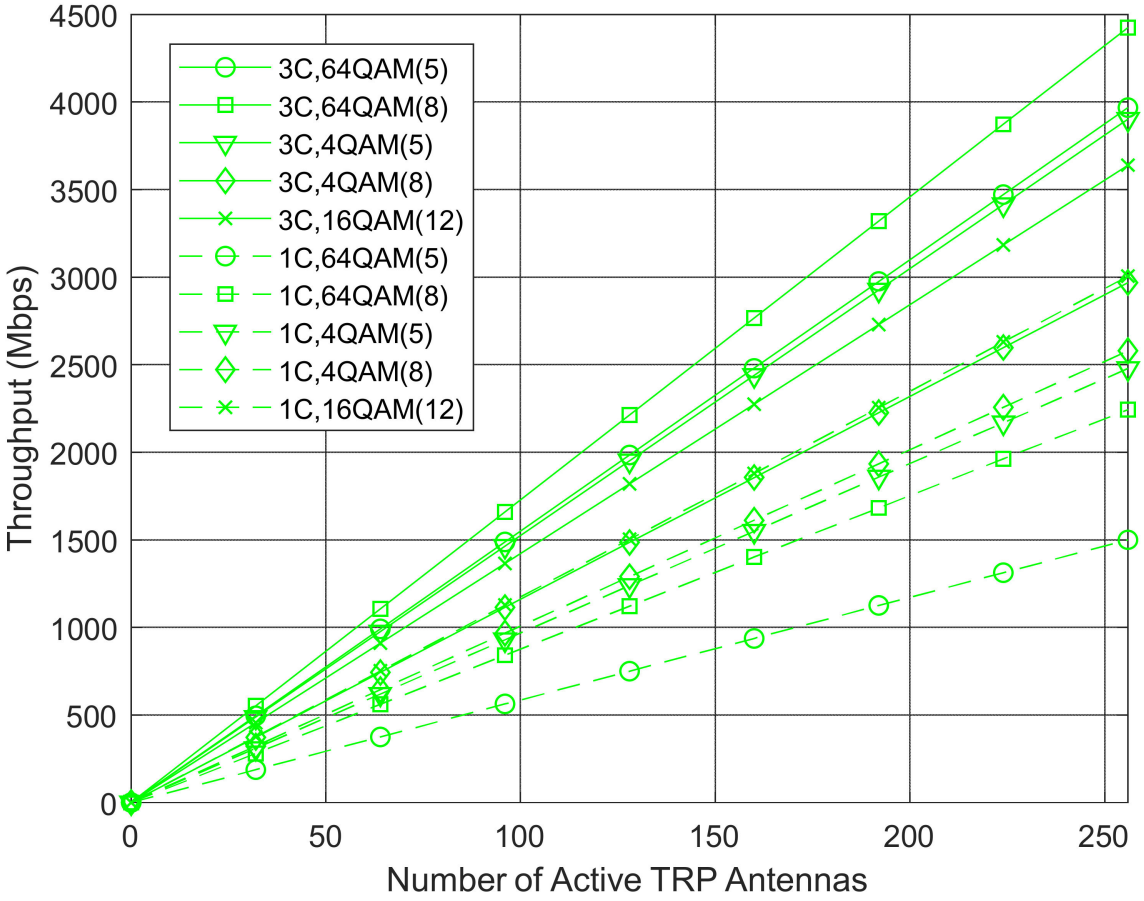

Figure 12. Throughput vs. number of active TRP antennas, for InD scenario, $N_{rx} = 5$, for two C-RAN cluster sizes, modulations and numbers of antennas per user, namely with $N_{tx}/N_u = 5$, 64QAM(5) and 4QAM(5); with $N_{tx}/N_u = 8$, 64QAM(8) and 4QAM(8); and with $N_{tx}/N_u = 12$, 16QAM(12).

From Figure 12, we conclude that the best N_{tx}/N_u depends on the C-RAN cluster size and modulation. For cluster size 1, the highest throughput performance continues to be that of $N_{tx}/N_u = 12$ using 16QAM, and the lowest throughput is obtained for 64QAM with

N_{tx}/N_u = 5. The high inter-interference of cluster size 1 makes high-order modulation with the maximum number of users served at the same time the worst case of achieved throughput. The case of 16QAM with N_{tx}/N_u = 12, in spite of having the minimum number of users served at the same time, has the highest bpcu per user and continues to present the lowest interference. For cluster size 3, there is much less inter-interference between sites, and the highest throughput performance is obtained for 64QAM with N_{tx}/N_u = 8. The lowest throughput is achieved for 4QAM with N_{tx}/N_u = 5. This is explained by the low-order modulation and lower bpcu associated with this case in spite of the maximum number of served users per site. Cluster size 3 has a small level of inter-interference and allows 64QAM with N_{tx}/N_u = 8 to achieve higher throughput than 64QAM with N_{tx}/N_u = 5, due to a higher bpcu despite a lower number of users per site. As before, we conclude that there is a value of N_{tx}/N_u that can achieve the highest throughput, but it depends on the cluster size and modulation. Higher N_{tx}/N_u with 16QAM is recommended for RAN cluster size 1 with a high level of inter-interference and a lower number of users per site. 64QAM with N_{tx}/N_u = 8 is recommended for RAN cluster size 3 with lower inter-interference but a higher number of users per site.

Table 2 presents the SE of the three scenarios, namely UMa, UMi and InD, for C-RAN cluster sizes of 1 and 3, based on the throughput results taken from Figures 10–12. It is observed that for cluster 1C, 16QAM(12) offers the highest SE for all scenarios. For cluster 3C, 64QAM(5) offers the highest SE for scenario UMi whereas 64QAM(8) offers the highest SE for scenario InD. For the UMa scenario, both 64QAM(5) and 64QAM(8) offer the highest SE.

Table 2. SE in bps/Hz of different scenarios and cluster sizes 1 and 3.

Modulation(SE)	UMa, 3C	UMi, 3C	InD, 3C	UMa, 1C	UMi, 1C	InD, 1C
64QAM(5)	2.00	2.75	1.55	0.51	0.61	0.59
64QAM(8)	2.00	2.29	1.73	0.65	0.98	0.88
4QAM(5)	1.76	1.84	1.52	0.66	0.90	0.97
4QAM(8)	1.36	1.38	1.16	0.71	0.80	1.00
16QAM(12)	1.69	1.71	1.42	0.88	1.06	1.17

In Figure 13, we compare the throughput for three different systems, namely the proposed PT-GSFIM, the BD MU-MIMO scheme from [37] and GSM MU-MIMO from [47], where we keep constant N_{tx}/N_u = 12 and N_{sc} = 256, resulting in approximately 12 bpcu. We evaluate the throughput for three scenarios, namely UMa, UMi and InD. We observe that independently of the system, the throughput performance of the InD scenario is the best, as expected. This is due to its double transmitted bit rate compared to the other scenarios; the combination of N_{tx}/N_u = 12 with cluster size 3 results in a smaller number of users and has lower inter-interference. Based on the results of Figure 13, the proposed PT-GSFIM scheme clearly outperforms both GSM and conventional MU-MIMO, taking advantage of the symbols being spread over a larger number of subcarriers, exactly N_f = 16 and N_{af} = 13, thus exploiting the frequency diversity.

Therefore, for C-RAN cluster size 3, both indoor and outdoor scenarios indicate that the total throughput achieved by our scheme is higher than that of conventional MU-MIMO and exhibits better system performance than the GSM counterpart.

In Figure 14, we compare the coverage of C-RAN cluster sizes 1 and 3 for 64QAM and 4QAM, both with N_{tx}/N_u = 8. As expected, the coverage of modulation 4QAM is higher than the coverage of 64QAM, independently of the cluster size. We also observe that for 100% of transmitted power, the coverage gain of cluster size 3 (3C) compared to cluster size 1 (1C) is 1.9 for 4QAM and increases to 3.1 for 64QAM. Cluster size 3 increases especially the coverage of high-order modulations such as 64QAM modulation.

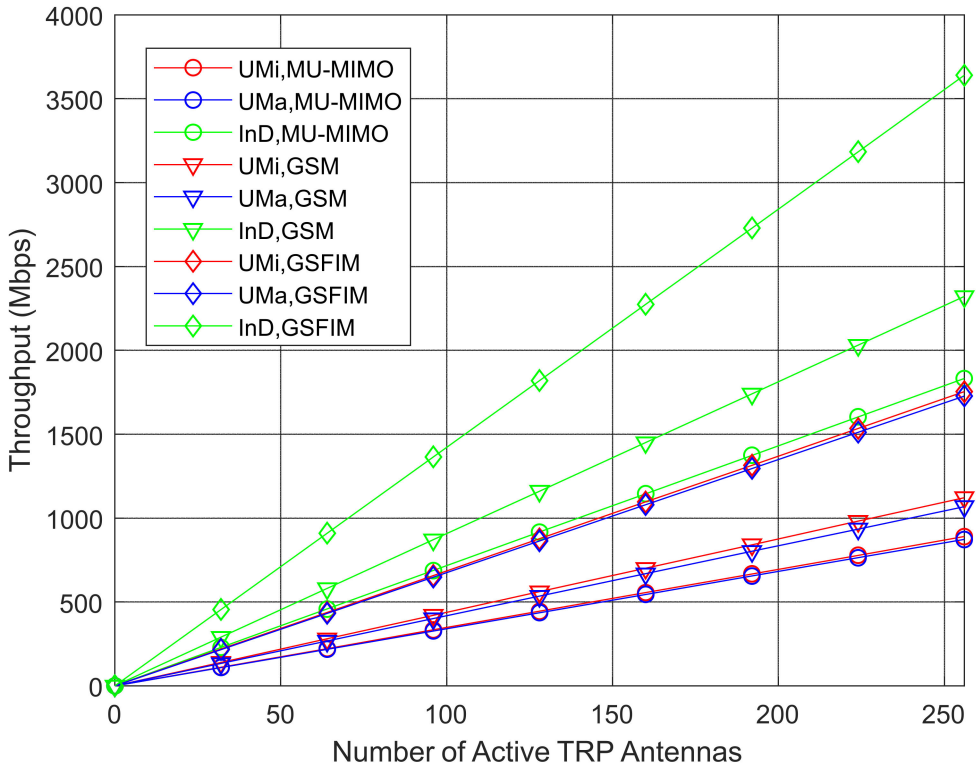

Figure 13. Throughput vs. number of active TRP antennas, RAN cluster size 3, for different systems and scenarios, with N_{tx}/N_u = 12, N_{sc} = 256, N_a = 2, N_{rx} = 5, 12 bpcu, GSM and MU-MIMO with 64QAM and GSFIM with 16QAM N_f = 16, N_{af} = 13.

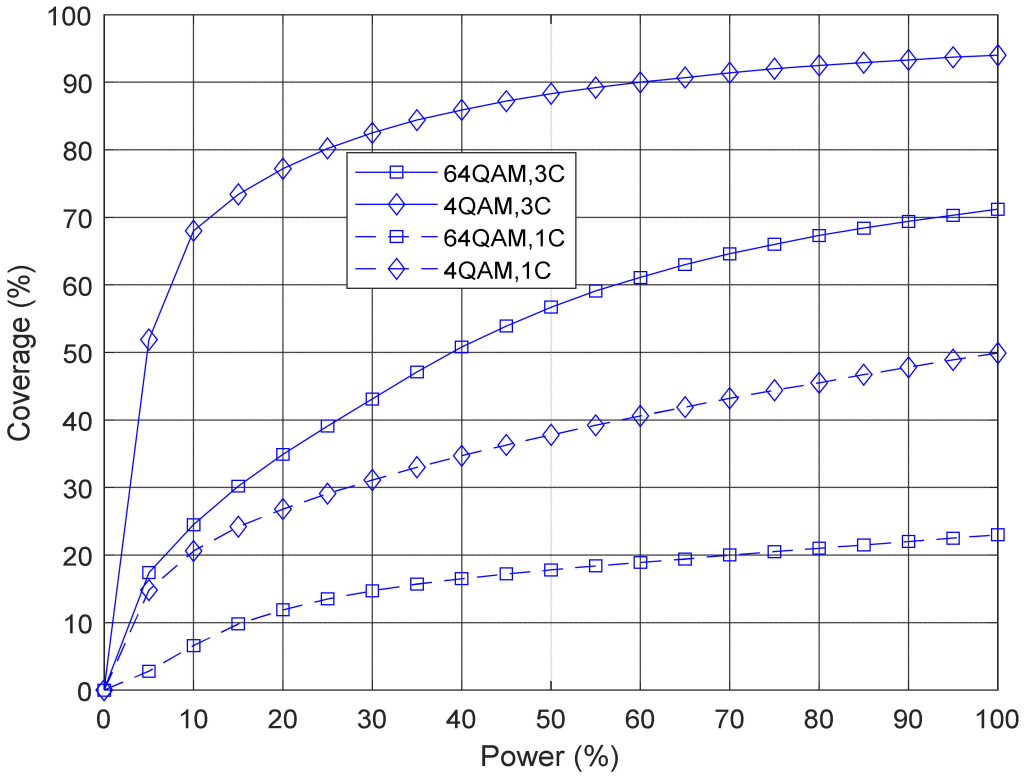

Figure 14. Coverage vs. percentage of TRP transmitted power, for UMa scenario, with N_{tx}/N_u = 8, N_{sc} = 256, N_{rx} = 5, 64QAM with 12.5 bpcu and 4QAM with 6.5 bpcu.

5. Conclusions

In this paper, we described a C-RAN aimed at 5G and beyond systems, where each BS transmits precoded space–frequency domain IM symbols. In the proposed approach, part of the information is conveyed implicitly on the indices of the active OFDM subcarriers and antennas, which also transmit normal APM signals carrying the remaining bits. The adopted PT-GSFIM scheme can benefit from the diversity effects inherent to frequency-selective channels and avoid inter-user interference at each receiver, which enables the C-RAN to accommodate flexible tradeoffs between SE, performance and complexity. A thorough system-level evaluation of the proposed PT-GSFIM-based C-RAN was performed considering standardized 5G NR scenarios with two different cluster sizes. With cluster size 3, the network is portioned into three adjacent TRP sets where each user is served by three TRPs, while the others perform inter-user interference. For RAN cluster size 1, we have the traditional cellular system. C-RAN system-level simulations considered three different three-dimensional scenarios using two different numerologies and frequency ranges: the UMa and UMi scenarios using numerology 1 at 3.5 GHz and the InD scenario using numerology 2 at 28 GHz. Throughput performance results indicate that, in spite of its higher bandwidth and higher achieved throughput, the 28 GHz band presents lower SE. The 3.5 GHz band having lower bandwidth and lower achieved throughput attains higher SE. There is an optimum number of transmitting antennas per user N_{tx}/N_u to achieve the highest throughput, but it depends on the cluster size of C-RAN and modulation. A higher number of N_{tx}/N_u with 16QAM is optimum for traditional cellular networks with a high level of intersite interference and a lower number of users per site. A lower number of N_{tx}/N_u with 64QAM is optimum for C-RAN with lower intersite interference but a higher number of users per site. Overall, the system evaluation shows that the proposed PT-GSFIM scheme can outperform both GSM and conventional MU-MIMO, exploiting its additional inherent frequency diversity. As future work, we intend to apply other alternative numerical and probabilistic methods which may be less time-intensive in order to achieve accurate system-level evaluation results.

Author Contributions: Conceptualization, V.V., J.P.P., N.S. and A.C.; methodology, V.V., J.P.P., N.S. and A.C.; software, V.V., J.P.P., C.R., C.G., N.S., P.S. and A.C; validation, V.V., J.P.P., C.R., C.G., N.S., P.S. and A.C.; formal analysis, V.V., J.P.P., C.R., C.G., N.S., P.S. and A.C.; investigation, V.V., J.P.P., C.R., C.G., N.S., P.S. and A.C.; resources, A.C. and N.S.; data curation, V.V., J.P.P., C.R., C.G., N.S., P.S. and A.C.; writing—original draft preparation, V.V., J.P.P., N.S. and A.C.; writing—review and editing, V.V., J.P.P., C.R., C.G., N.S., P.S. and A.C.; visualization, V.V., J.P.P., C.R., C.G., N.S., P.S. and A.C.; supervision, A.C. and N.S.; project administration, A.C. and N.S.; funding acquisition, A.C. and N.S. All authors have read and agreed to the published version of the manuscript.

Funding: This work was supported by the Fundação para a Ciência e Tecnologia (FCT) under the grant 2020.05621.BD. The authors also acknowledge the funding provided by FCT/MCTES through national funds and when applicable co-funded EU funds under the project UIDB/50008/2020.

Institutional Review Board Statement: Not applicable.

Informed Consent Statement: Not applicable.

Data Availability Statement: The data presented in this study are available on request from the corresponding author. The data are not publicly available due to privacy.

Conflicts of Interest: The authors declare no conflict of interest.

References

1. 3rd Generation Partnership Project (3GPP). TS 38.101 v14.1.1, 5GNR. User Equipment (UE) radio transmission and reception, Release 15, August 2017. Available online: https://3gpp.org/ftp/Specs/archive/38_series/38.101-1/38101-1-001.zip (accessed on 7 January 2022).
2. Marques da Silva, M.; Dinis, R. Power-Ordered NOMA with Massive MIMO for 5G Systems. *Appl. Sci.* **2021**, *11*, 3541. [CrossRef]
3. Basar, E.; Wen, M.; Mesleh, R.; Di Renzo, M.; Xiao, Y.; Haas, H. Index Modulation Techniques for Next-Generation Wireless Networks. *IEEE Access.* **2017**, *5*, 16693–16746. [CrossRef]

4. Basar, E. Index modulation techniques for 5G wireless networks. *IEEE Commun. Mag.* **2016**, *54*, 168–175. [CrossRef]
5. Cheng, X.; Zhang, M.; Wen, M.; Yang, L. Index Modulation for 5G: Striving to Do More with Less. *IEEE Wirel. Commun.* **2018**, *25*, 126–132. [CrossRef]
6. Correia, A.; Souto, N.; Sebastiao, P.; Gomez-Barquero, D.; Fuentes, M. Broadcasting Scalable Video with Generalized Spatial Modulation in Cellular Networks. *IEEE Access.* **2020**, *8*, 22136–22144. [CrossRef]
7. Dogan Tusha, S.; Tusha, A.; Basar, E.; Arslan, H. Multidimensional Index Modulation for 5G and Beyond Wireless Networks. *Proc. IEEE.* **2021**, *109*, 170–199. [CrossRef]
8. Mesleh, R.; Haas, H.; Sinanovic, S.; Ahn, C.W.; Yun, S. Spatial Modulation. *IEEE Trans. Veh. Technol.* **2008**, *57*, 2228–2241. [CrossRef]
9. Younis, A.; Serafimovski, N.; Mesleh, R.; Haas, H. Generalised spatial modulation. In Proceedings of the Conference Record of the Forty Fourth Asilomar Conference on Signals, Systems and Computers, Pacific Grove, CA, USA, 7–10 November 2010; pp. 1498–1502.
10. Zhang, R.; Yang, L.; Hanzo, L. Generalised Pre-Coding Aided Spatial Modulation. *IEEE Trans. Wirel. Commun.* **2013**, *12*, 5434–5443. [CrossRef]
11. Basar, E.; Aygolu, U.; Panayirci, E.; Poor, H. Orthogonal Frequency Division Multiplexing with Index Modulation. *IEEE Trans. Signal. Processing* **2013**, *61*, 5536–5549. [CrossRef]
12. Basar, E. On Multiple-Input Multiple-Output OFDM with Index Modulation for Next Generation Wireless Networks. *IEEE Trans. Signal. Processing* **2016**, *64*, 3868–3878. [CrossRef]
13. Li, J.; Wen, M.; Jiang, X.; Duan, W. Space-Time Multiple-Mode Orthogonal Frequency Division Multiplexing with Index Modulation. *IEEE Access.* **2017**, *5*, 23212–23222. [CrossRef]
14. Gao, S.; Zhang, M.; Cheng, X. Precoded Index Modulation for Multi-Input Multi-Output OFDM. *IEEE Trans. Wirel. Commun.* **2018**, *17*, 17–28. [CrossRef]
15. Xiao, Y.; Wang, S.; Dan, L.; Lei, X.; Yang, P.; Xiang, W. OFDM With Interleaved Subcarrier-Index Modulation. *IEEE Commun. Lett.* **2014**, *18*, 1447–1450. [CrossRef]
16. Li, J.; Dang, S.; Wen, M.; Jiang, X.; Peng, Y.; Hai, H. Layered Orthogonal Frequency Division Multiplexing with Index Modulation. *IEEE Syst. J.* **2019**, *13*, 3793–3802. [CrossRef]
17. Mao, T.; Wang, Z.; Wang, Q.; Chen, S.; Hanzo, L. Dual-Mode Index Modulation Aided OFDM. *IEEE Access.* **2017**, *5*, 50–60. [CrossRef]
18. Mao, T.; Wang, Q.; Wang, Z. Generalized Dual-Mode Index Modulation Aided OFDM. *IEEE Commun. Lett.* **2017**, *21*, 761–764. [CrossRef]
19. Wen, M.; Basar, E.; Li, Q.; Zheng, B.; Zhang, M. Multiple-Mode Orthogonal Frequency Division Multiplexing with Index Modulation. *IEEE Trans. Commun.* **2017**, *65*, 3892–3906. [CrossRef]
20. Wen, M.; Li, Q.; Basar, E.; Zhang, W. Generalized Multiple-Mode OFDM With Index Modulation. *IEEE Trans. Wirel. Commun.* **2018**, *17*, 6531–6543. [CrossRef]
21. Althunibat, S.; Mesleh, R.; Rahman, T. A Novel Uplink Multiple Access Technique Based on Index-Modulation Concept. *IEEE Trans. Commun.* **2019**, *67*, 4848–4855. [CrossRef]
22. Basar, E. Media-Based Modulation for Future Wireless Systems: A Tutorial. *IEEE Wirel. Commun.* **2019**, *26*, 160–166. [CrossRef]
23. Souto, N.; Correia, A. Frequency Domain Equalization for Single and Multiuser Generalized Spatial Modulation Systems in Time Dispersive Channels. *IEEE Wirel. Commun. Lett.* **2020**, *9*, 316–320. [CrossRef]
24. Datta, T.; Eshwaraiah, H.; Chockalingam, A. Generalized Space-and-Frequency Index Modulation. *IEEE Trans. Veh. Technol.* **2016**, *65*, 4911–4924. [CrossRef]
25. Velez, V.; Pavia, J.; Souto, N.; Sebastiao, P.; Correia, A. A Generalized Space-Frequency Index Modulation Scheme for Downlink MIMO Transmissions with Improved Diversity. *IEEE Access.* **2021**, *9*, 118996–119009. [CrossRef]
26. Wang, L.; Chen, Z.; Gong, Z.; Wu, M. Space-Frequency Coded Index Modulation with Linear-Complexity Maximum Likelihood Receiver in the MIMO-OFDM System. *IEEE Signal Processing Lett.* **2016**, *23*, 1439–1443. [CrossRef]
27. Zaidi, S.; Ben Smida, O.; Affes, S.; Vilaipornsawai, U.; Zhang, L.; Zhu, P. User-Centric Base-Station Wireless Access Virtualization for Future 5G Networks. *IEEE Trans. Commun.* **2019**, *67*, 5190–5202. [CrossRef]
28. 3rd Generation Partnership Project (3GPP). TS 38.211 v15.2.0. 5G/NR Physical Channels and Modulation, (Release 15). 2018. Available online: https://3gpp.org/ftp/Specs/archive/38_series/38.211/38211-f30.zip. (accessed on 30 September 2021).
29. 3rd Generation Partnership Project (3GPP). TS 38.214; NR.; Physical layer procedures for data, (Release 15). 2020. Available online: https://3gpp.org/ftp/Specs/archive/38_series/38.214/38214-fb0.zip. (accessed on 30 September 2021).
30. 3rd Generation Partnership Project (3GPP). TS 38.213; NR.; Physical layer procedures for control, (Release 15). 2020. Available online: https://3gpp.org/ftp/Specs/archive/38_series/38.213/38213-fb0.zip. (accessed on 30 September 2021).
31. Zaidi, A.; Baldemair, R.; Tullberg, H.; Bjorkegren, H.; Sundstrom, L.; Medbo, J.; Kilinc, C.; Da Silva, I. Waveform and Numerology to Support 5G Services and Requirements. *IEEE Commun. Mag.* **2016**, *54*, 90–98. [CrossRef]
32. Begishev, V.; Samuylov, A.; Moltchanov, D.; Machnev, E.; Koucheryavy, Y.; Samouylov, K. Connectivity Properties of Vehicles in Street Deployment of 3GPP NR Systems. In Proceedings of the 2018 IEEE Globecom Workshops (GC Wkshps), Abu Dhabi, United Arab Emirates, 9–13 December 2018.

33. Gkonis, P.; Trakadas, P.; Kaklamani, D. A Comprehensive Study on Simulation Techniques for 5G Networks: State of the Art Results, Analysis, and Future Challenges. *Electronics* **2020**, *9*, 468. [CrossRef]
34. Lakshmi Narasimhan, T.; Chockalingam, A. On the Capacity and Performance of Generalized Spatial Modulation. *IEEE Commun. Lett.* **2016**, *20*, 252–255. [CrossRef]
35. 3rd Generation Partnership Project (3GPP). TR 38.913 5G.; Study on scenarios and requirements for next generation access technologies, version 16.0.0 Release 16, July 2020. Available online: https://3gpp.org/ftp/Specs/archive/38_series/38.913/38913-g00.zip (accessed on 18 November 2021).
36. 3rd Generation Partnership Project (3GPP). TR 38.901 Study on channel model for frequencies from 0.5 to 100 GHz (Release 14). 2017. Available online: https://3gpp.org/ftp/Specs/archive/38_series/38.901/38901-e20.zip (accessed on 30 September 2021).
37. 3rd Generation Partnership Project (3GPP). TR 36.873 Study on 3D channel model for LTE (Release 12), 2014. Available online: https://3gpp.org/ftp/Specs/archive/36_series/36.873/36873-c00.zip (accessed on 30 September 2021).
38. Spencer, Q.; Swindlehurst, A.; Haardt, M. Zero-Forcing Methods for Downlink Spatial Multiplexing in Multiuser MIMO Channels. *IEEE Trans. Signal. Processing* **2004**, *52*, 461–471. [CrossRef]
39. Souto, N.; Correia, A. A Precoding Aided Space Domain Index Modulation Scheme for Downlink Multiuser MIMO Systems. *IEEE Trans. Veh. Technol.* **2020**, *69*, 12333–12337. [CrossRef]
40. Pavia, J.; Velez, V.; Ferreira, R.; Souto, N.; Ribeiro, M.; Silva, J.; Dinis, R. Low Complexity Hybrid Precoding Designs for Multiuser mmWave/THz Ultra Massive MIMO Systems. *Sensors* **2021**, *21*, 6054. [CrossRef] [PubMed]
41. Boutros, J.; Viterbo, E. Signal space diversity: A power- and bandwidth-efficient diversity technique for the Rayleigh fading channel. *IEEE Trans. Inf. Theory* **1998**, *44*, 1453–1467. [CrossRef]
42. Correia, A. Optimized Complex Constellations for Transmitter Diversity. *Wirel. Pers. Commun. J.* **2002**, *20*, 267–284.
43. Lopes, H.; Souto, N. Iterative Signal Detection for Large-Scale GSM-MIMO Systems. *IEEE Trans. Veh. Technol.* **2018**, *67*, 7734–7738. [CrossRef]
44. Van Chien, T.; Björnson, E. Massive MIMO Communications. In *5G Mobile Communications*; Xiang, W., Zheng, K., Shen, X., Eds.; Springer: Berlin, Germany, 2017.
45. Correia, A.; Silva, M.M. Link and system level simulation for MIMO. In *MIMO Processing for 4G and Beyond: Fundamentals and Evolution*; Silva, M.M., Monteiro, F.A., Eds.; CRC Press: Boca Raton, FL, USA, 2014.
46. Pavia, J.; Velez, V.; Brogueira, B.; Souto, N.; Correia, A. Precoded Generalized Spatial Modulation for Downlink MIMO Transmissions in Beyond 5G Networks. *Appl. Sci.* **2020**, *10*, 6617. [CrossRef]
47. Xiao, Y.; Yang, Z.; Dan, L.; Yang, P.; Yin, L.; Xiang, W. Low-Complexity Signal Detection for Generalized Spatial Modulation. *IEEE Commun. Lett.* **2014**, *18*, 403–406. [CrossRef]